JOURNAL OF GEOPHYSICAL RESEARCH, VOL. 99, NO. E12, PAGES 25,993–26,013, DECEMBER 25, 1994

Thermal and albedo mapping of the polar regions of Mars using Viking thermal mapper observations
2. South polar region

David A. Paige and Kenneth D. Keegan
Department of Earth and Space Sciences, University of California, Los Angeles

Abstract. We present the first maps of the apparent thermal inertia and albedo of the south polar region of Mars. The observations used to create these maps were acquired by the infrared thermal mapper (IRTM) instruments on the two Viking Orbiters over a 30-day period in 1977 during the Martian late southern summer season. The maps cover the region from 60°S to the south pole at a spatial resolution of 1° of latitude, thus completing the initial thermal mapping of the entire planet. The analysis and interpretation of these maps is aided by the results of a one-dimensional radiative convective model, which is used to calculate diurnal variations in surface and atmospheric temperatures, and brightness temperatures at the top of the atmosphere for a range of assumptions concerning dust optical properties and dust optical depths. The maps show that apparent thermal inertias of bare ground regions decrease systematically from 60°S to the south pole. In unfrosted regions close to the south pole, apparent thermal inertias are among the lowest observed anywhere on the planet. On the south residual cap, apparent thermal inertias are very high due to the presence of CO_2 frost. In most other regions of Mars, best fit apparent albedos based on thermal emission measurements are generally in good agreement with actual surface albedos based on broadband solar reflectance measurements. However, in the frost-free region poleward of 75°S, best fit apparent albedos are significantly higher than measured Lambert albedos, implying that measured brightness temperatures in this area are up to 15 K colder than would be expected for surfaces with the same measured albedos during this season. The one-dimensional atmospheric model calculations also predict anomalously cold brightness temperatures close to the pole during late summer, and after considering a number of alternatives, it is concluded that the net surface cooling due to atmospheric dust is the best explanation for this phenomenon. The observed systematic decrease in apparent thermal inertia from 60°S to the south pole during this season is also consistent with the predictions of atmospheric model calculations. The region of lowest apparent thermal inertia close to the pole, which includes the south polar layered deposits, is interpreted to be mantled by a continuous layer of aeolian material that must be at least a few millimeters thick. The low thermal inertias mapped in the south polar region imply an absence of surface water ice deposits, which is consistent with Viking Mars atmospheric water detector (MAWD) measurements which show low atmospheric water vapor abundances throughout the summer season. However, these observations do not necessarily imply a complete absence of water. Thermal model calculations that can reproduce observed diurnal temperature variations in the south polar region show that annual maximum subsurface temperatures at depths ranging from 4 to 20 cm are cold enough to permit the stability of ground ice deposits, even if they are in excellent diffusive contact with the atmosphere. Therefore, the presence of near-surface ground ice in the south polar region is not inconsistent with the Viking IRTM and MAWD observations.

1. Introduction

In Paper 1 [*Paige et al.,* this issue], we presented the first maps of the apparent thermal inertia and albedo of the north polar region of Mars. In this paper, we present the results of a similar study of the south polar region. These maps, plus the midlatitude maps of *Kieffer et al.* [1976a] and *Palluconi and Kieffer* [1981] complete the initial mapping of the entire planet.

Paper number 93JE03429.
0148-0227/94/93JE-03429$05.00

When comparing the known properties of the south polar region of Mars to those of the north, one is struck by the many differences. On average, the south polar region is higher in elevation, and is more heavily cratered. Unlike the north, it does not contain extensive circumpolar dune deposits, but it does contain extensive areas of exposed layered deposits [*Murray et al.,* 1972; *Thomas et al.*, 1992]. Due to the eccentricity of the Martian orbit, the spring and summer seasons in the south are shorter but more intense than their northern counterparts. The southern spring and summer seasons are also the most likely periods for great dust storm activity [*Zurek*, 1982]. The residual polar cap in the south is much smaller than the residual cap in the north, and is offset from the geographic pole. During the years of

Mariner 9 and Viking observations, the south residual cap contained CO_2 frost even at the end of summer [*Kieffer*, 1979; *Paige and Ingersoll*, 1985; *Paige et al.*, 1990], whereas at the same season, the north residual cap contained only water ice [*Kieffer et al.*, 1976b]. Unlike the north, the south polar region did not contain abundant atmospheric water vapor during the summer season of 1977 [*Farmer and Doms*, 1979; *Davies and Wainio*, 1981]. However, abundant water vapor was detected by ground-based observations during the southern summer season of 1969, which has been interpreted as evidence for the exposure of water ice deposits at the south residual cap [*Jakosky and Barker*, 1984].

Given these many differences, one might be tempted to predict at the outset that the thermal properties of the south polar region of Mars should be different from those in the north. In the next section, we describe the procedures we have used to map the apparent thermal and reflectance properties of the south polar region of Mars, and describe the results. In the section that follows, we explore the sensitivity of these results to the potential effects of the Martian atmosphere, which are not considered when creating the maps. In the final section, we interpret all our results in terms of surface physical properties, and geological and atmospheric processes.

2. Mapping Apparent Thermal Inertia and Albedo

The basic procedures we have used to map the apparent thermal inertia and albedo of the south polar region of Mars are similar to those described in Paper 1.

Selection and Processing of IRTM Observations

During the southern summer season of 1977, conditions in the Martian south polar region were not as ideal for thermal mapping as they were during the northern summer season of 1978 when the maps in Paper 1 were produced. During 1977, Viking observed two global dust storms. The first storm (1977A) started at L_s 207, the second storm (1977B) started at L_s 272. Infrared thermal mapper (IRTM) observations at the south residual cap show that there was a relatively clear period in late spring that occurred between the global dust storms near L_s 250 [*Paige and Ingersoll*, 1985]. Unfortunately, large portions of the region southward of 75°S were still covered by the retreating south seasonal CO_2 polar cap during this season [*James et al.*, 1979], which would have prevented observations of diurnal surface temperature variations in these areas. The most suitable period for south polar mapping occurred in the late southern summer, when the seasonal CO_2 polar cap was approaching its residual configuration, and the 1977B dust storm had largely dissipated [*Martin et al.*, 1979; *Pollack et al.*, 1979]. To map the south polar region, we used IRTM 20-μm channel (T_{20}) observations obtained during a 30-day period from August 24, 1977, to September 23, 1977 (L_s 321.58 to 338.07, Julian date 2443380 to 2443410).

The mapping regions used in this study were larger than those used in Paper 1 because the IRTM observations of the south polar region were obtained at longer slant ranges than those in the north. The IRTM observations from both orbiters were constrained to exclude observations obtained at slant ranges of less than 6500 km and greater than 33,000 km, and emission angles of greater than 78.464°. Approximately 30% of these observations were obtained at slant ranges of less than 11,000 km, and 80% were obtained at slant ranges of less than 15,000 km. If the IRTM field of view is taken to be a circle with a diameter of 5.2 mrad [*Chase et al.*, 1978], then the minor axes of the unsmeared fields ranged from 33 to 172 km when projected on the planet. The remaining observations were then grouped into 3238 mapping regions with boundaries defined by squares with sides of 1° of latitude on a simple polar conic projection, where r=(90° - latitude) and θ=(90°+ longitude). As in Paper 1, the choice of region sizes was dictated by trade-offs between coverage, instrument field of view, and the desire to make maps with the best possible spatial resolution. The areas of the mapping regions used in this study are 4 times those used to map the north polar region in Paper 1, and one quarter those used by *Palluconi and Kieffer* [1981] to map the midlatitude regions from 60°S to 60°N. The total number of observations used was 124,913.

Determining Best Fit Apparent Thermal Inertias and Albedos

Using a basic thermal model that does not include the effects of the atmosphere (see Paper 1), we created a five-dimensional table of model-calculated surface temperatures in the south polar region as a function of latitude, season, local time, soil albedo, and thermal inertia. CO_2 frost albedos were fixed at 0.55, which provided a good fit to the observed retreat of the south seasonal polar cap along the 225° meridian [*James et al.*, 1979; *Kieffer et al.*, 1979]. During the 30-day mapping period, surface temperatures in the south polar region decreased by approximately 25 K as the subsolar point moved from 15.1°S to 8.9°S. This variation was well resolved in the south polar interpolation table, which used a seasonal resolution of 5 sols, and a latitude resolution of 2° south of 80°S, and 5° northward of 80°S. As in Paper 1, the table used a local time resolution of one Mars hour, a soil albedo resolution of 0.1, and a thermal inertia resolution of 41.86 J $m^{-2} s^{-1/2} K^{-1} \times \times 2^n$ where n assumed all integer values from 0 to 6. Using the least squares fitting procedures described in Paper 1, best fit apparent thermal inertias I^* and best fit apparent albedos A^* were determined for each mapping region that had more than five T_{20} observations.

Apparent Thermal Inertia and Albedo Maps

Plates 1 and 2 show maps of the best fit apparent thermal inertia I^* and best fit apparent albedo A^* for the IRTM south polar observations used in this study. The maps of both quantities show interesting structure. At all longitudes, apparent thermal inertias decrease gradually from 60°S to the south pole. Most of the unfrosted regions poleward of 80°S have low apparent thermal inertias. Very high apparent inertias are mapped at the south residual cap centered at 87°S, 45°W, which still contained CO_2 frost during the mapping period [*Kieffer*, 1979; *James et al.*, 1979; *Paige and Ingersoll*, 1985]. High apparent thermal inertias are also mapped in an elongated frost outlier centered at 84°S, 15°W, which was just disappearing according to Viking Orbiter images obtained during the mapping period [*James et al.*, 1979; *Herkenhoff and Murray*, 1990]. Most unexpectedly, best fit apparent albedos increase dramatically from 75°S to the south pole. The regions of highest best fit albedos appear to be centered on the south residual cap. Very high best fit albedos are also mapped on the elongated frost outlier.

Figures 1 and 2 show the number of T_{20} observations per mapping region and the standard deviations of the best fits. For

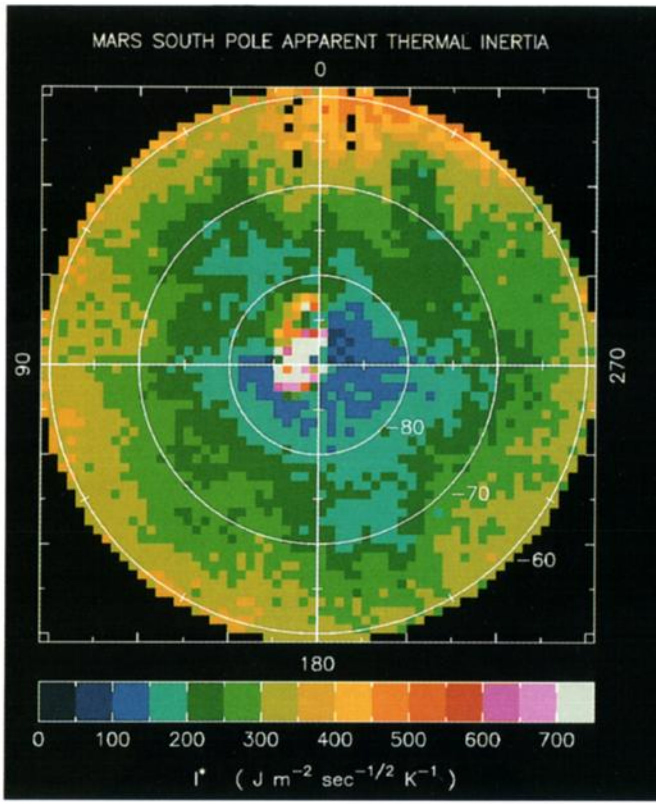

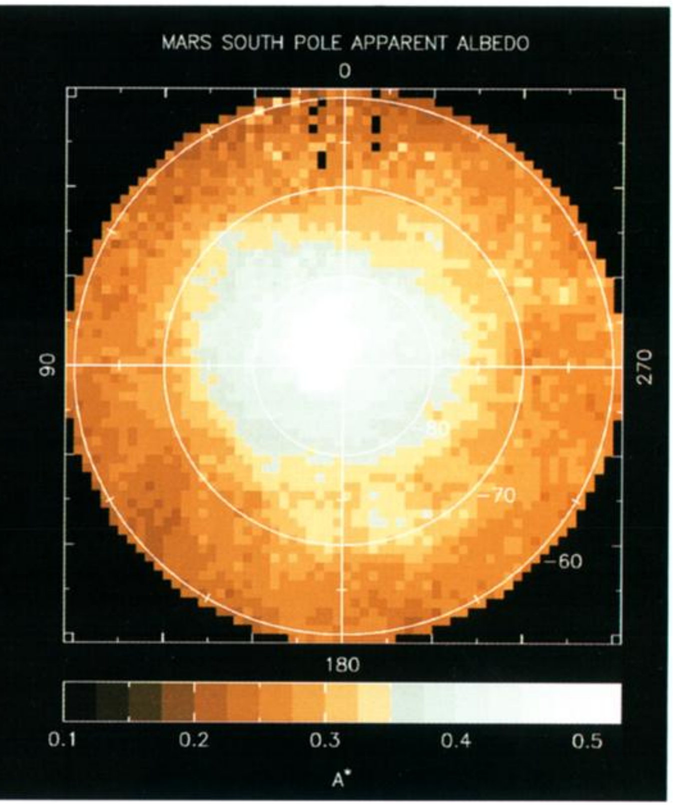

Plate 1. Best fit apparent thermal inertians I^* for the region from 60°S to the south pole. Regions with $I^* > 700$ J m^{-2} s$^{-1/2}$ K^{-1} are colored gray.

Plate 2. Best fit apparent albedos A^* for the region from 60°S to the south pole.

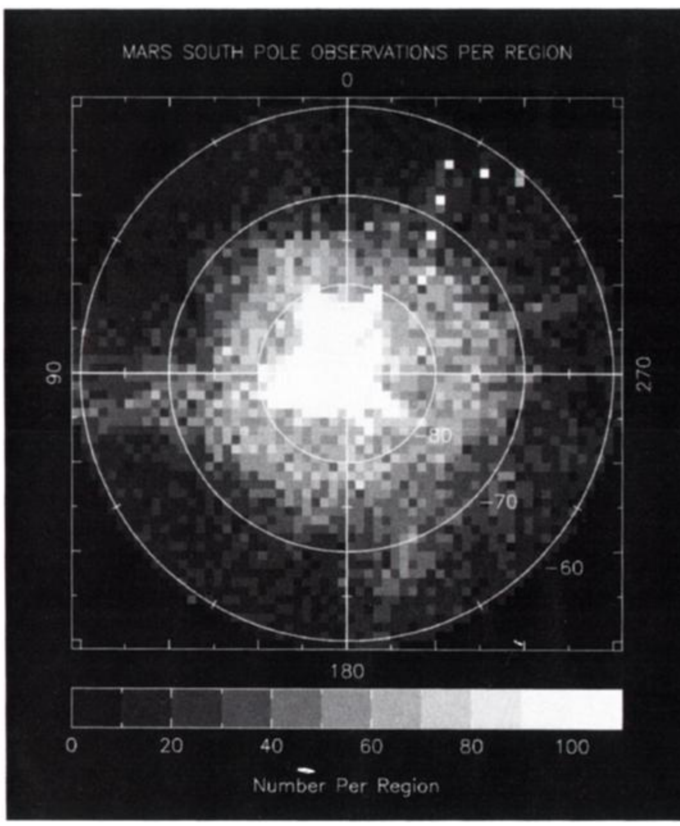

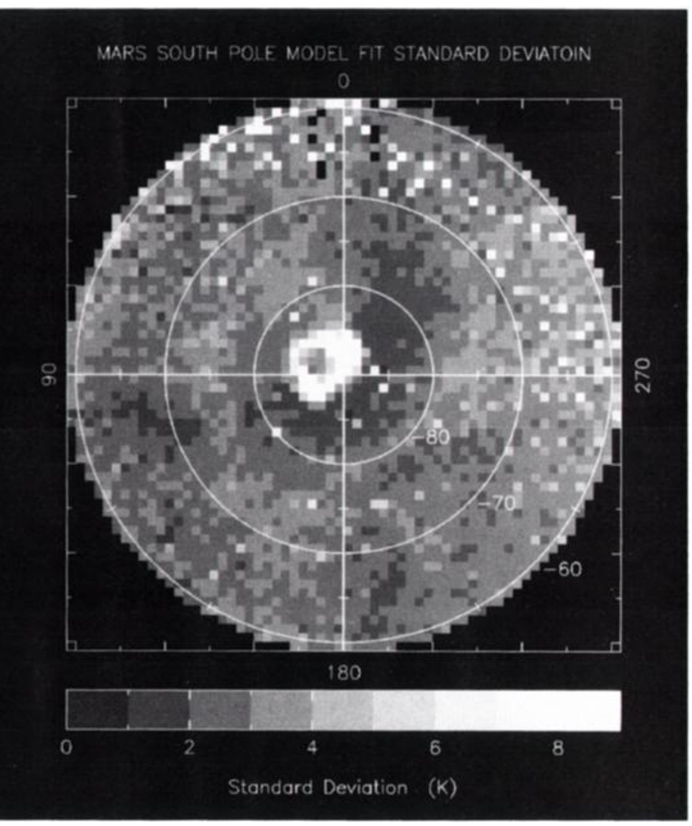

Figure 1. Number of IRTM T_{20} observations for the region from 60°S to the south pole.

Figure 2. Standard deviations of best fit σ^* for the region from 60°S to the south pole.

most regions, the standard deviations were less than 3 K. The major exceptions were regions on or near the south residual cap which contained CO_2 frost. Since CO_2 frost solid-vapor equilibrium temperatures are fixed at 148 K, the extremely small diurnal temperature variations observed in these regions could not be successfully fit by the basic thermal model, which assumed all seasonal CO_2 frost had completely sublimated earlier in the season. Therefore, the very high best fit thermal inertias and albedos that are mapped in the south residual cap region are artifacts, and should not be interpreted as measures of polar cap thermal or reflectance properties.

Comparisons With Measured Albedos

During the mapping period, the Viking IRTM instruments acquired an extensive set of broadband solar reflectance observations of the south polar region [*Kieffer*, 1979]. As in Paper 1, we have used the IRTM solar channel observations to map the Lambert albedo at solar zenith angles of less than 85°.

Plate 3 shows A_L, the average measured Lambert albedo for solar zenith angles of less than 85° for all regions that had more than one observation. This map presents a much more realistic picture of the visual appearance of the south polar region during late summer than does the apparent albedo map in Figure 2. Plate 4 shows the quantity A_L-A^* which is the difference between the averaged measured Lambert albedo based on IRTM solar channel measurements and the best fit apparent albedo based on T_{20} measurements. At latitudes north of 70°S, best fit apparent albedos are in good agreement with measured Lambert albedos. Poleward of 70°S, best fit apparent albedos become progressively higher than measured Lambert albedos. Away from the residual polar cap, the difference between A_L and A^* appears to be symmetric with longitude. At the residual cap itself, A^* is much greater than A_L due to the presence of cold CO_2 frost.

Figure 3 shows a cross plot of A^* versus A_L for all regions. The distribution of points in Figure 3 can be divided into three regions. The first is a region of diagonally distributed points that lie along the A^*=A_L line, which were obtained northward of 70°S which show a good agreement between best fit and Lambert albedos. The second is an adjacent region of vertically distributed points which were obtained in the unfrosted regions poleward of 70°S for which A_L is approximately 0.25 and A^* ranges from 0.25 to 0.45. The third is a relatively small number of diagonally distributed points which were obtained on and adjacent to the south residual polar cap, for which A_L ranged from 0.25 to 0.5, and A^* ranged from 0.45 to 0.8. The behavior shown in Figure 3 is very different from that observed in the north polar region, where A^* was in much better agreement with with A_L (see Paper 1).

Comparison With Previous Results

Palluconi and Kieffer [1981] used IRTM observations to map the apparent thermal inertia of Mars from 60°S to 60°N at a spatial resolution of 2° of latitude by 2° of longitude. Figure 4a shows a comparison between best fit apparent thermal inertias for regions between 58°S and 60°S from *Palluconi* and *Kieffer* [1981] and from this study. Figure 4b shows a comparison between measurement of A_g the "phase-corrected" albedo from IRTM solar channel measurements from *Pleskot and Miner* [1982], and A^*, the best fit apparent albedo from this study. The best fit albedos mapped in this study are in excellent agreement

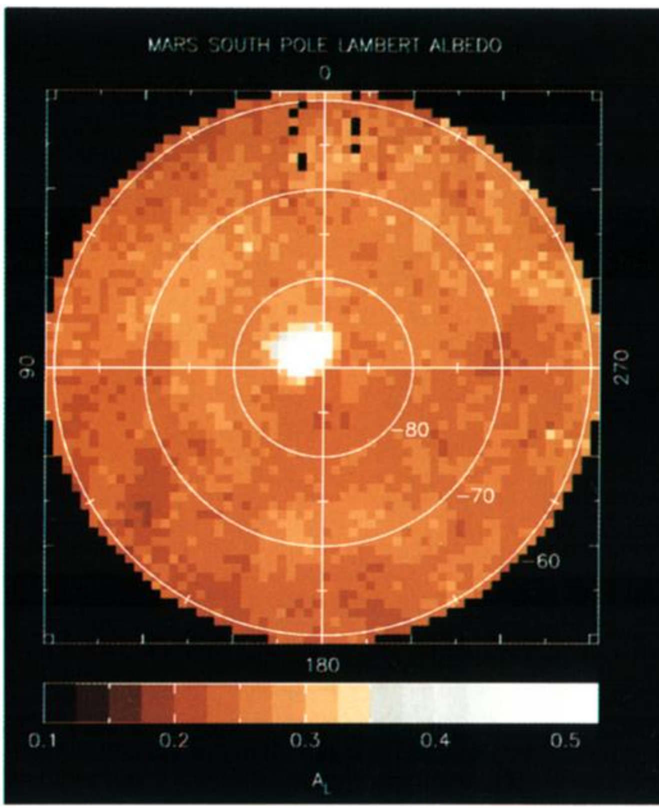

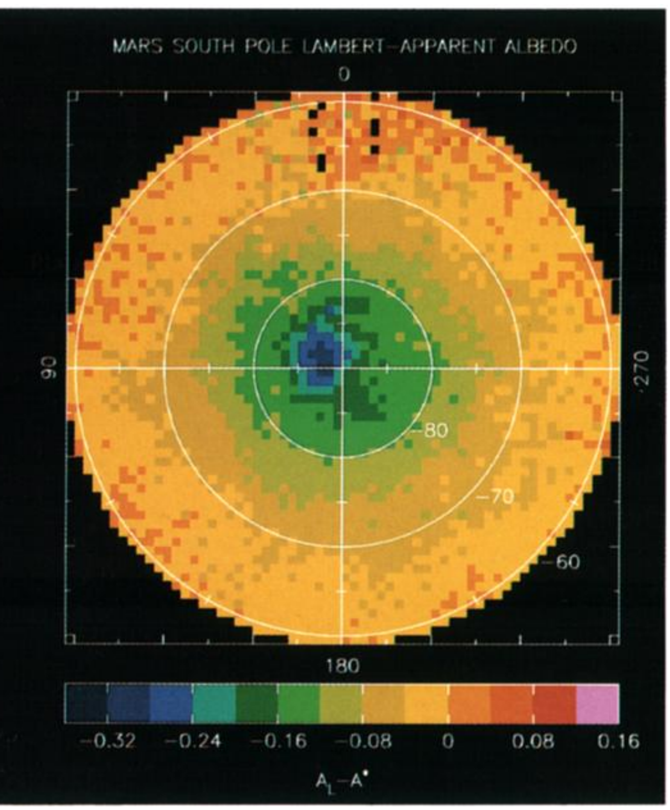

Plate 3. Average Lambert albedo A_L for the region from 60°S to the south pole.

Plate 4. Difference between Lambert albedo and best fit apparent albedo A_L - A^* for the region from 60°S to the south pole.

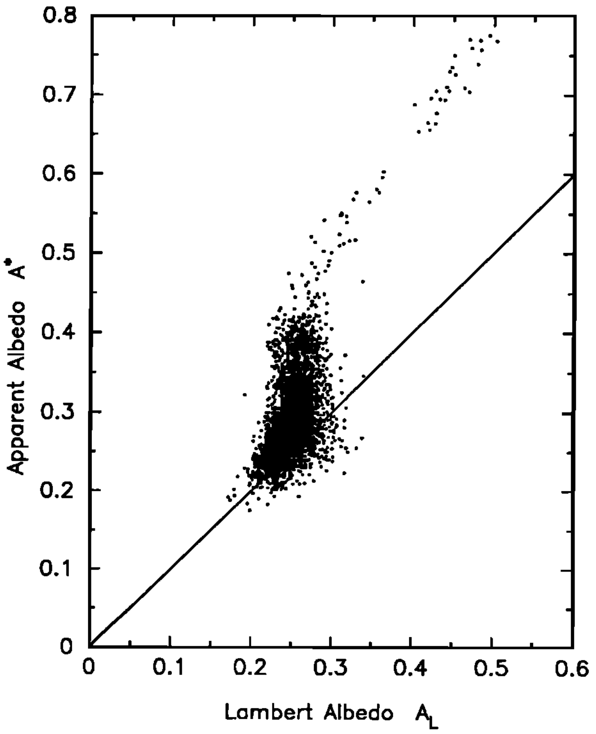

Figure 3. Cross plot of best fit apparent albedo A^* versus measured average Lambert albedo A_L for all regions mapped.

with the measured albedos of *Pleskot and Miner* [1982]. The apparent thermal inertias mapped in this study are systematically higher than those of *Palluconi and Kieffer* [1981]. This is likely due to the fact that the *Palluconi and Kieffer* [1981] map was created using IRTM observations obtained between L_s 344 and 125, which was after the observations used in this study were obtained. By L_s 344, the 1977B global dust storm had completely cleared, which should have resulted in lower dust opacities and lower apparent thermal inertias. Given the strong sensitivity of apparent inertia to dust opacity [*Pollack et al.*, 1979; *Palluconi and Kieffer*, 1981; *Haberle and Jakosky*, 1991; Paper 1], a systematic increase in apparent thermal inertia like that indicated in Figure 4a could easily be explained by a temporal variation in dust opacity.

Figure 5 shows cross plots of A^* versus I^* for the regions mapped. In unfrosted regions, there is a clear anticorrelation between apparent albedo and apparent thermal inertia. Figure 6 shows cross plots of A_L versus I^* for the regions mapped. In dark regions, there is much less of a correlation between Lambert albedo and apparent thermal inertia, although the range of variation of both quantities is rather small. In bright regions containing CO_2 frost, there is a suggestion of a weak correlation between both apparent and Lambert albedo, and apparent thermal inertia.

South Polar Temperatures

Determining best fit values for I^* and A^* for a given region makes it possible to use the basic thermal model to compute temperature variations over a complete diurnal cycle. Plates 5 and 6 show maps of computed daily minimum and maximum surface temperatures (using basic thermal model fits to the IRTM T_{20} measurements) midway through the mapping period at Julian date 2443395 (L_s 330). The effects of latitude, season, and the presence of CO_2 frost are all evident. At the south residual polar cap, both minimum and maximum temperatures remain fixed at the CO_2 frost point of approximately 148 K. Daily minimum and maximum temperatures increase sharply in the unfrosted regions surrounding the residual cap. Maximum temperatures increase steadily towards the equator, while minimum temperatures increase both equatorward and poleward of 75°S.

Figure 7a shows best fit model-calculated daily minimum, maximum, and average temperatures as a function of latitude midway through the mapping period for the IRTM observations obtained along the 45° to 225° meridian, which bisects the south residual cap. For comparison, Figure 7a also shows these same quantities calculated for homogenous flat surfaces with albedos of 0.25 and thermal inertias of 150 and 300 J m^{-2} s$^{-1/2}$ K^{-1}. Figure 7a demonstrates the degree to which measured brightness temperatures in the south polar region are colder than would be predicted by the basic thermal model. Along the 225°W meridian, lower than expected temperatures are observed at latitudes as low as 75°S. Close to the south pole where diurnal surface temperature variations nearly vanish, measured brightness temperatures are more than 15 K colder than would be expected for surfaces with the same Lambert albedos. At the bright core region of the residual polar cap itself, measured brightness temperatures are close to the CO_2 frost point, and show very small diurnal variations. The true range of diurnal

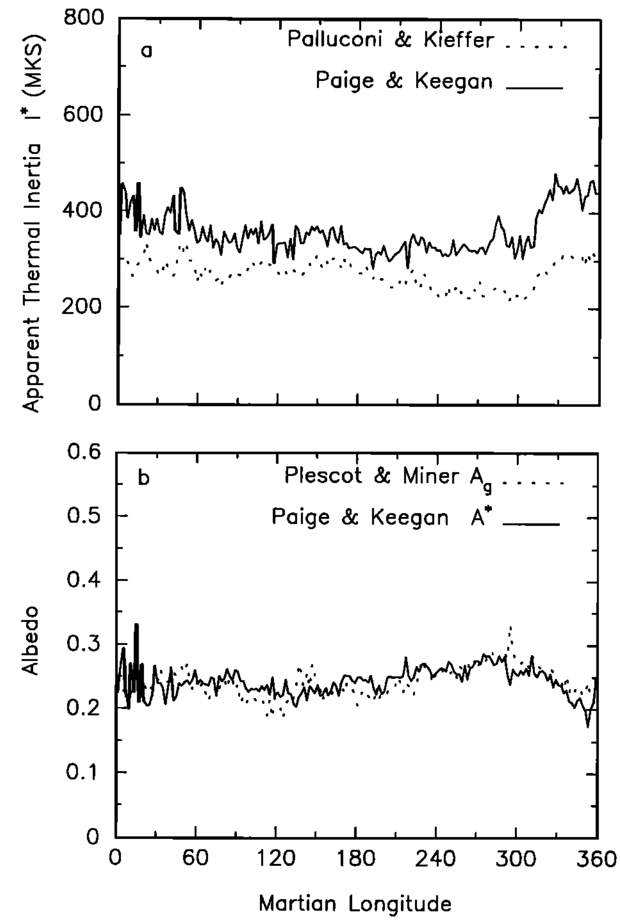

Figure 4. Comparison between the results presented in Plates 1 and 2, and those of previous studies for regions between 58°N and 60°N as a function of longitude. (a) Apparent thermal inertia I^* from Figure 1, and I^* from *Palluconi and Kieffer* [1981]. (b) Best fit apparent albedo A^* from Figure 2, and "phase-corrected" albedo A_g from *Pleskot and Miner* [1982].

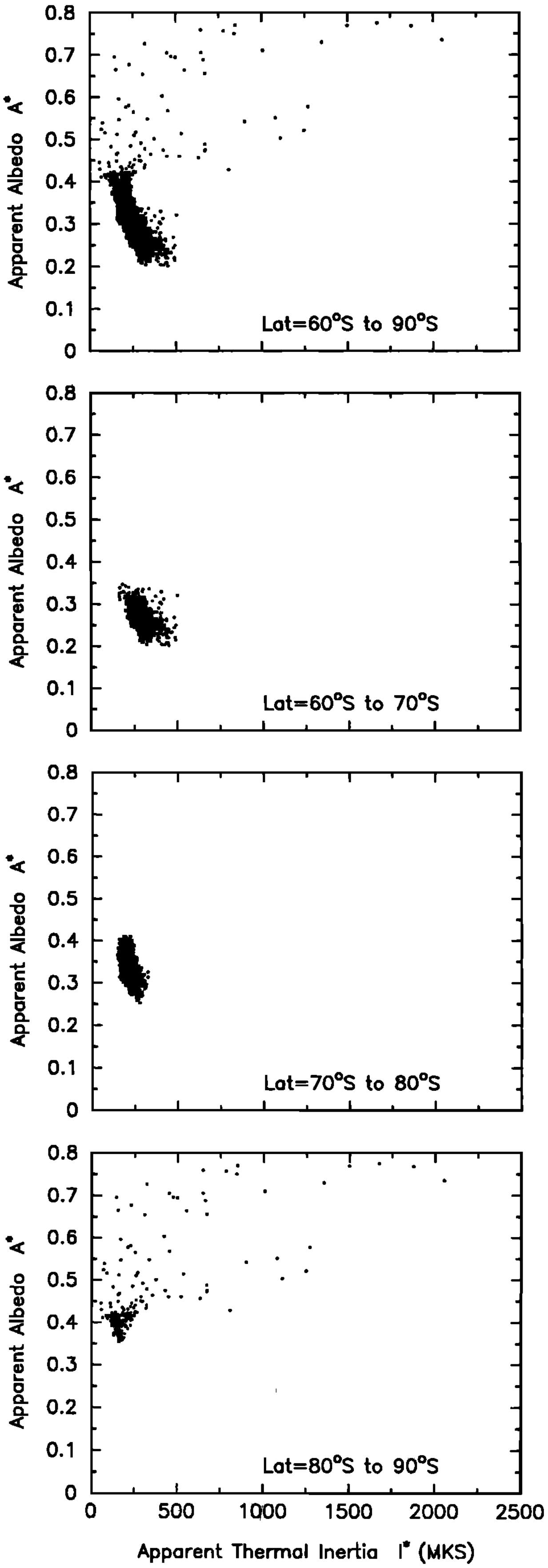

Figure 5. Cross plots of best fit apparent albedo A^* versus best fit apparent thermal inertias I^* for the regions indicated.

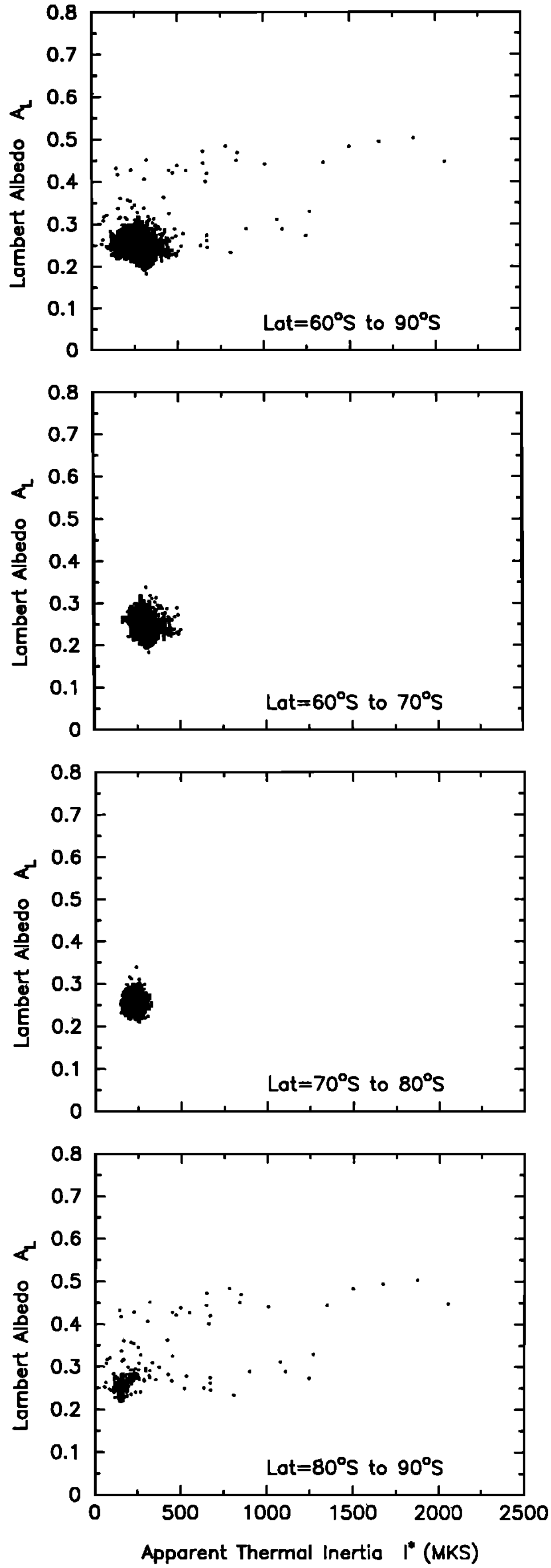

Figure 6. Cross plots of average Lambert albedo A_L versus best fit apparent thermal inertias I^* for the regions indicated.

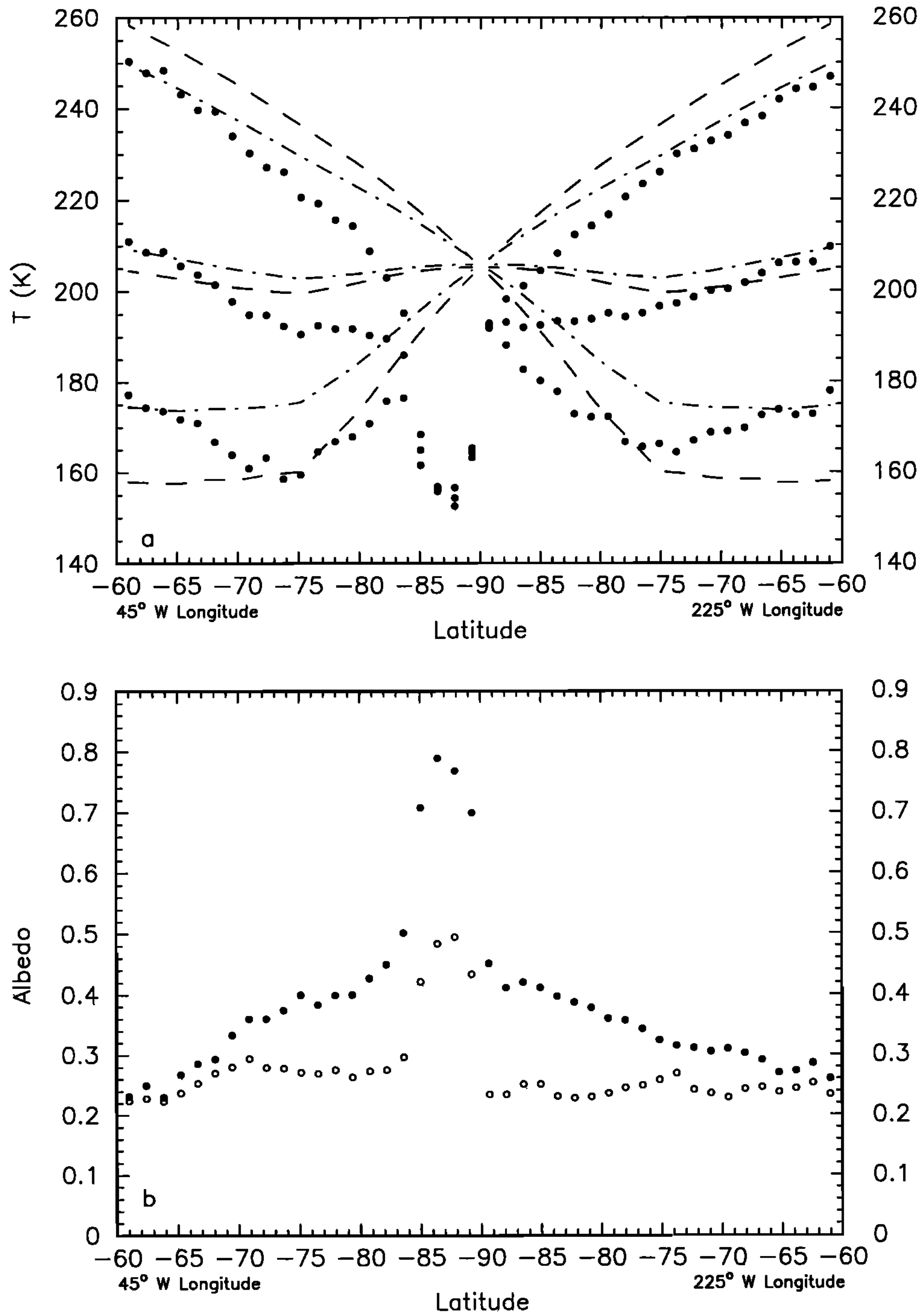

Figure 7. Profiles of model-calculated quantities midway through the mapping period as a function of latitude along the 45°W to 225°W meridians, which bisect the south residual polar cap. (a) The solid dots are best fit computed daily minimum, maximum, and average surface temperatures from IRTM 20-μm channel brightness temperatures. The dashed lines are basic thermal model calculated minimum, maximum, and average temperatures assuming a surface albedo of 0.25 and a surface thermal inertia of 150 J m^{-2} s$^{-1/2}$ K^{-1}. The dot-dashed lines are the same for a surface thermal inertia of 300 J m^{-2} s$^{-1/2}$ K^{-1}. (b) The solid dots are best fit apparent albedos A^*, the open dots are average Lambert albedos A_L.

temperature variations for these regions is difficult to estimate because the standard deviations of the best fits in these regions are larger than the range of best fit calculated temperature variations (see Figure 2). Along the 45°W meridian from 80°S to 60°S, measured minimum, maximum and average temperatures nearly mirror those obtained along the 225° meridian. These trends are also apparent in Figure 7b, which shows best fit and Lambert albedos along the same meridians.

Residual Diurnal Variability

Although it was possible to obtain values for I^* and A^* that provided a good fit to the IRTM T_{20} observations for most

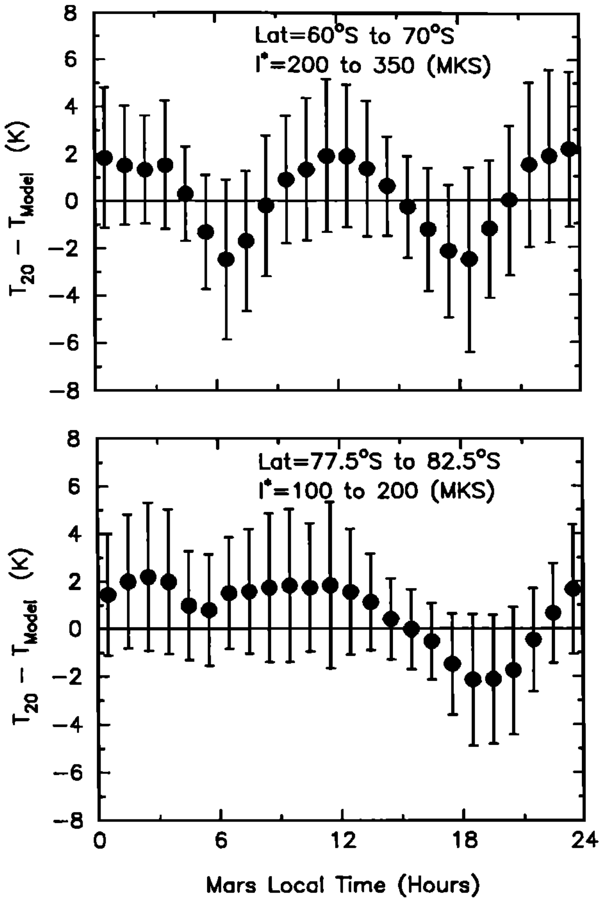

Figure 8. Average differences between observed values of T_{20} and best fit model-calculated surface temperatures as a function of Mars local time for the regions and apparent thermal inertia ranges indicated. Standard deviations are indicated by vertical bars.

regions, systematic residual differences remained. Figure 8 shows average differences between T_{20} and best fit model-calculated surface temperatures as a function of Mars local time. Figure 8 (top) includes all data for all regions between 60°S and 70°S with I^* between 200 and 350 J m^{-2} s$^{-1/2}$ K^{-1}. Figure 8 (bottom) includes all data for all regions between 77.5°S and 82.5°S with I^* between 100 and 200 J m^{-2} s$^{-1/2}$ K^{-1}. In both cases, the pattern of residual diurnal variability is similar, with T_{20} being more than 2 K lower than the best fit model predictions in the late afternoon, which is reminiscent of the "anomalous afternoon cooling phenomenon" observed at lower latitudes [*Ditteon*, 1982]. The amplitudes of these residual diurnal variations are greater than those observed in the north polar region (see Paper 1). This contributes to the somewhat higher standard deviations of the fits to the IRTM south polar observations. The 4 K amplitude of the residual diurnal variation shown in Figure 8 (bottom) is quite significant, given that the total amplitude of the diurnal variation observed at 80°S was approximately 21 K (see Figure 7).

Discussion

The south polar thermal and albedo mapping results presented here have revealed what appears to be a large thermal anomaly. In all other frost-free areas of Mars that have been mapped to date, there has been a reasonably good agreement between best

Table 1. Model Atmosphere Properties

Model Atmosphere	Aerosol Solar Parameters				Aerosol IR Refractive Index Data	Size Distribution Parameters			Aerosol Vertical Distribution, mbar	Comments
	τ_{so}	Q_{ext}	ϖ_0	g		r_m	α	γ		
0	-	-	-	-	---	-	-	-	-	No atmosphere
1	0.0	-	-	-	---	-	-	-	-	CO_2 gas but no aerosols
2	0.2	2.74	0.79	0.86	Mariner 9-inferred dust	0.4	2	0.5	6.0 - 0.0	Standard dust case τ_{so}=0.2
3	0.6	2.74	0.79	0.86	Mariner 9-inferred dust	0.4	2	0.5	6.0 - 0.0	Standard dust case τ_{so}=0.6
4	0.2	2.74	0.92	0.55	Mariner 9-inferred dust	0.4	2	0.5	6.0 - 0.0	*Clancy and Lee* [1991] dust
5	0.2	2.74	0.79	0.86	Mariner 9-inferred dust	0.4	2	1.0	6.0 - 0.0	Smaller dust particles
6	0.6	2.74	0.79	0.86	Mariner 9-inferred dust	0.4	2	1.0	6.0 - 0.0	Smaller dust particles
7	0.6	2.74	0.79	0.86	Mariner 9-inferred dust	0.4	2	1.0	6.0 - 3.6	Smaller dust confined to lowest two scale heights
8	1.2	2.74	0.79	0.86	Mariner 9-inferred dust	0.4	2	1.0	6.0 - 0.0	Smaller dust particles with high opacity

τ_{so}, Q_{ext}, ϖ_0 and g are the solar spectrum averaged aerosol optical depth extinction efficiency single scattering albedo and asymmetry parameter, r_m is the mode radius and α and γ are shape parameters for modified gamma particle size distributions [*Deirmendjian* 1969]

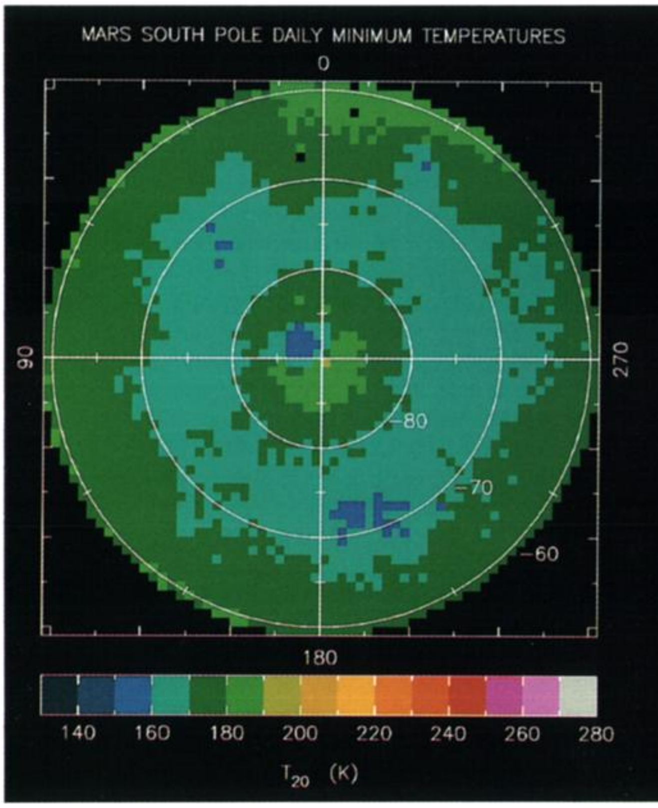

Plate 5. Map of computed daily minimum surface temperatures (as measured by T_{20}) at Julian date 2443395 (L_s 330) using best fit values for I^* and A^* as inputs to the basic thermal model.

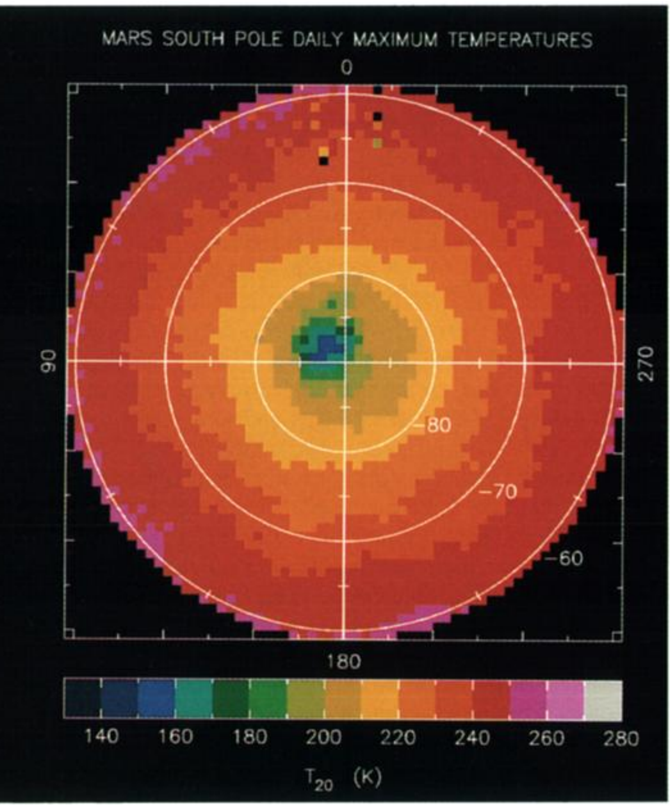

Plate 6. Map of computed daily maximum surface temperatures (as measured by T_{20}) at Julian date 2443395 (L_s 330) using best fit values for I^* and A^* as inputs to the basic thermal model.

fit apparent albedos based on thermal emission measurements, and actual surface albedos based on broadband solar reflectance measurements [*Kieffer et al.*, 1977; *Paige*, 1992; Paper 1]. However, in the dark, apparently frost-free region poleward of 75°S, best fit apparent albedos are significantly higher than measured Lambert albedos during the late summer season. The difference is greatest at the highest latitudes. In the region surrounding the south residual polar cap, measured brightness temperatures are as much as 15 K colder than would be expected for flat surfaces in radiative equilibrium.

In Paper 1, a one-dimensional radiative-convective model was used to demonstrate that the Martian atmosphere can have a number of significant effects in the north polar region. In the next section, we present an analogous set of model calculations for the south polar region, paying particular attention to atmospheric effects that could potentially be responsible for the south polar thermal anomaly. In the section that follows, we use this information to aid in the interpretation of our apparent thermal inertia and albedo maps.

3. The Effects of the Atmosphere

We have used the one-dimensional radiative-convective model described in Paper 1 to investigate the potential effects of the Martian atmosphere on south polar surface temperatures, and on observed radiances at the top of the atmosphere. In Paper 1, we considered the sensitivity of the model results to the effects of variations in atmospheric properties and surface thermal inertia. In this paper, we explore how these effects vary with season using a set of model atmospheres that provide a representative sampling of possible dust optical properties and optical depths in the south polar region.

Model Calculations

The model was run for nine different combinations of atmospheric properties at six latitudes from 60°S to 85°S. All calculations assumed a soil thermal inertia I=83.72 J m^{-2} s$^{-1/2}$ K^{-1}, a soil albedo A_s=0.25, a CO_2 frost albedo of 0.55, and a CO_2 frost emissivity of 1.0. Table 1 shows the nine sets of model atmosphere properties used in the calculations. For model atmosphere 0, the atmosphere was assumed to be nonexistent. The results for model atmosphere 0 are identical to those of the basic thermal model. For model atmosphere 1, the atmosphere was assumed to contain CO_2 gas, but no aerosols. For model atmosphere 2, the atmosphere was assumed to contain dust distributed uniformly with pressure, with solar spectrum averaged optical properties like those inferred at the Viking 1 landing site during the 1977B global dust storm [*Pollack et al.*, 1979]. At infrared wavelengths, the dust was assumed to have montmorillonite 219B refractive indices from 5 to 15 μm [*Toon et al.*, 1977], and basalt refractive indices from 15 to 50 μm [*Pollack et al.*, 1973], which provided a good fit to Mariner 9 infrared interferometer spectrometer (IRIS) observations during the 1971A global dust storm [*Toon et al.*, 1977], and to observations obtained by IRTM [*Hunt*, 1979]. Dust infrared optical properties were calculated using Mie theory [*Hansen and Travis*, 1974] assuming a modified gamma size distribution [*Deirmendjian*, 1969] with the size parameters r_m=0.4, α=2, and γ=0.5. These dust optical properties have been used commonly in previous calculations, and in this paper will be referred to as "Mariner 9-inferred" dust. Model atmosphere 2 assumes a solar spectrum averaged normal optical depth τ_{so} of 0.2. Model atmosphere 3 assumes an optical depth of τ_{so} 0.6. Model atmosphere 4 assumes Mariner 9-inferred dust optical properties at infrared wavelengths, but uses solar spectrum averaged optical properties derived by *Clancy and Lee* [1991] from IRTM emission phase function observations, with an optical depth τ_{so} of 0.2. Model atmospheres 5 through 8 assume standard Viking Lander dust solar spectrum averaged dust optical properties [*Pollack et al.*, 1979], but use a dust size distribution that is more sharply peaked at the smaller radii. This decreases the ratio of the solar to infrared dust opacity by a factor of 2. Model atmosphere 5 assumes a dust optical depth τ_{so} of 0.2. Model atmosphere 6 assumes a dust optical depth τ_{so} of 0.6. Model atmosphere 7 uses the same dust optical properties as Model atmosphere 6, but assumes that the dust is uniformly distributed between the surface and the 3.6-mbar pressure level, which leaves the atmosphere free of dust at altitudes greater than approximately 15 km. Model atmosphere 8 assumes that the dust is distributed uniformly with pressure, with an optical depth τ_{so} of 1.2.

For all cases, the model was run for three Mars years without a radiatively active atmosphere as with the basic thermal model to equilibrate subsurface temperatures until Julian date 2443315 (L_s 283.0). By this time, the Viking observations show that the retreating south seasonal CO_2 cap was approaching its residual configuration [*James et al.*, 1979], and the basic thermal model predicts the complete disappearance of seasonal CO_2 frost. At this point, the atmosphere was "turned on" and the results were recorded 20 days later at Julian date 2443395 (L_s 295), and 80 days later at Julian date 2443395 (L_s 330), which is midway through the mapping period. The consideration of a soil with relatively low thermal inertia minimizes the potential effects of the different model atmospheres on the behavior of the seasonal polar cap, and on seasonal variations in soil temperatures themselves.

Results

Figure 9 shows a number of one-dimensional model-calculated quantities at L_s 295 as a function of latitude for the eight model atmospheres. The results at 60°S and 80°S are presented in numerical form in Table 2. These calculations were performed before the start of the mapping period during the early southern summer season, when the subsolar latitude was 22.5°S. From the standpoint of solar geometry, these calculations are analogous to the early northern summer calculations presented in Paper 1. The general character of the results is similar to those in the north. During early southern summer, atmospheric dust reduces the amplitudes of diurnal temperature variations and increases apparent thermal inertias. When the effects of dust on brightness temperatures at the top of the atmosphere are properly included, apparent thermal inertias are increased even further. For a constant dust opacity, the effects of dust on apparent thermal inertia are somewhat greater at lower latitudes than they are near the poles. Under clear atmospheric conditions, the 15-μm band of CO_2 gas is responsible for a mild greenhouse effect. The addition of dust tends to decrease the effectiveness of the CO_2 greenhouse, particularly at the highest latitudes. All these effects are discussed in greater detail in Paper 1.

Figure 10 shows the same one-dimensional model-calculated quantities later in the summer at L_s 330, which is midway through the mapping period. The results at 60°S and 80°S are presented in numerical form in Table 3. Calculated temperatures at all latitudes are lower during this season because the subsolar latitude had moved northward to 12.2°S. Comparison between the results in Figures 9b and 10b shows that dust has nearly the same effects on calculated apparent thermal inertias during both seasons. Comparison between the results in Figures 9c and 10c shows that dust has very different effects on calculated best fit apparent albedos. During early summer, calculated best fit apparent albedos are generally less than or equal to actual surface albedos. The only exception occurs poleward of 70°S for model atmosphere 8, which assumes the highest dust optical depth. During late summer, calculated best fit apparent albedos increase from 60°S to the pole. Near the pole, calculated best fit apparent albedos can be as much as 0.1 higher than calculated planetary albedos at the same latitudes (see Figure 10g). Figure 10d shows that adding dust to the south polar atmosphere during this season significantly lowers calculated daily average temperatures. The magnitude of the dust antigreenhouse effect is greatest at the highest latitudes. For model atmosphere 8, which assumes a solar spectrum averaged dust optical depth of 1.2, the dust cooling effect is almost 16 K at 85°S. Comparison between the results for model atmospheres 2 and 3 and for model atmospheres 5 and 6 shows that the magnitude of the dust cooling effect is enhanced for dust size distributions that assume smaller particles. Comparison between the results for model atmospheres 6 and 7 shows that confining the dust to the lowest two scale heights does not significantly alter the dust antigreenhouse effect.

The potential cooling effects of atmospheric dust on surface temperatures that are implied by the one-dimensional model results presented in this paper have been documented in a number of previous studies. *Davies* [1979] used a simple radiative equilibrium model to explore the effects of dust on the heating of the surface and atmosphere of Mars as a function of solar spectrum averaged dust optical properties, surface albedo, and solar zenith angle. The net effect of atmospheric dust on surface heating depends on competing effects at solar and infrared wavelengths. At solar wavelengths, dust heats the atmosphere and reduces downgoing solar fluxes at the surface. At infrared wavelengths, enhanced thermal emission from the dust-heated atmosphere increases downgoing infrared fluxes at the surface. *Davies* [1979] showed that in radiative equilibrium, the net effect of atmospheric dust is to cool surfaces with low albedos and to warm surfaces with high albedos. For every combination of dust optical properties, dust opacity, and solar zenith angle, there is a unique "break-even" albedo, for which the addition of dust to the atmosphere has no net effect on surface heating rates. For typical dust optical properties, *Davies*' [1979] calculations show that for solar zenith angles of 0° to 60°, the break-even albedo is close to 0.45. For higher solar zenith angles, the break-even albedo increases dramatically, which implies that for unfrosted bare-ground surfaces, the net cooling effect of atmospheric dust is enhanced at high solar zenith angles. This trend is clearly evident in the more detailed calculations presented in Figures 9 and 10. The effects of aerosols on surface temperatures have also been investigated in the terrestrial context. Of particular relevance to the work presented in this paper are studies of the effects of persistent stratospheric dust or smoke layers [*Cess et al.*, 1985; *Turco et al.*, 1991]. One-dimensional "nuclear winter" calculations show that the net cooling effect of dark aerosol clouds on surface temperatures increases as the ratio of the cloud's infrared to visible optical depth decreases [*Turco et al.*, 1991]. This trend is also evident in the results for model

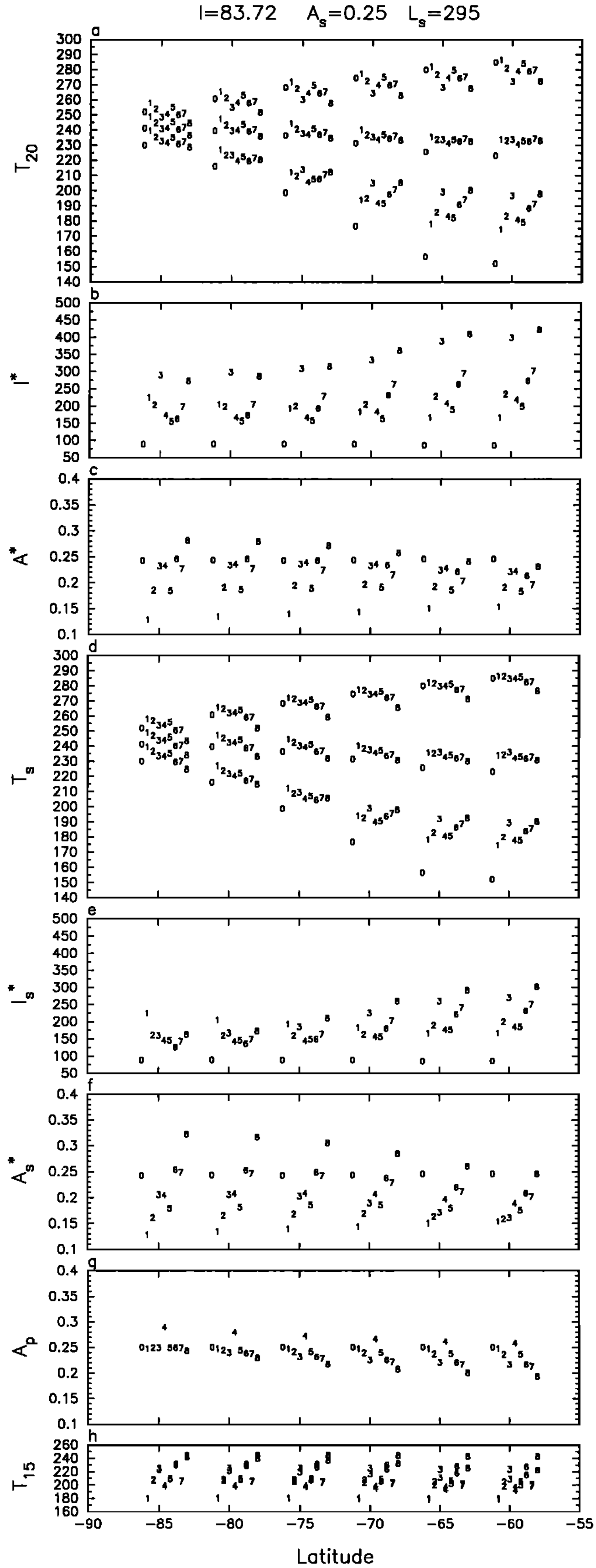

Figure 9. One-dimensional radiative-convective model results as a function of latitude before the start of the mapping period at L_s 295. Numeric symbols represent the results for the corresponding model atmospheres in Table 1. The symbols are offset horizontally from their true latitudes at -60°, -65°, -70°, -75°, -80°, and -85° for clarity. The surface thermal inertia was assumed to be 83.72 J m^{-2} s$^{-1/2}$ K^{-1}, and the surface albedo was assumed to be 0.25 for all cases. (a) Daily minimum, maximum and average IRTM 20-μm channel brightness temperatures at the top of the atmosphere for cos e = 0.75. (b) Best fit apparent thermal inertia I^* using one-dimensional model-calculated IRTM 20-μm channel brightness temperatures at the top of the atmosphere. Model atmosphere zero is the basic thermal model, which assumes no atmosphere is present. (c) Best fit apparent albedo A^* using one-dimensional model calculated IRTM 20-μm channel brightness temperatures at the top of the atmosphere, and the basic thermal model. (d) Daily minimum, maximum, and average surface temperatures T_s . (e) Best fit apparent thermal inertia I_s^* using one-dimensional model-calculated surface temperatures, and the basic thermal model. (f) Best fit apparent albedo A_s^* using one-dimensional model-calculated surface temperatures, and the basic thermal model. (g) Planetary albedo A_p at the top of the atmosphere. (h) One-dimensional model-calculated IRTM 15-μm channel brightness temperatures at the top of the atmosphere at cos e = 0.75 at 5 hours, and 17 hours Mars local time.

atmospheres 6 and 7, which assume lower infrared to visible optical depth ratios than model atmospheres 2 and 3.

Figure 11 shows one-dimensional model calculations of the quantity (T_{20} - T_{Model}) as a function of Mars local time at 65°S and 80°S midway through the mapping period. For model atmospheres 2 through 8, the patterns of calculated residual diurnal variability are very similar to those observed by IRTM, especially at 80°S (see Figure 8). The ability of the one-dimensional model to predict these residual diurnal variations lends support to the hypothesis that they are due largely to atmospheric phenomena [*Haberle and Jakosky*, 1991]. It also provides some degree of confidence in the realism of the one-dimensional model calculations themselves.

The IRTM 15-μm channel brightness temperatures (T_{15}) provide measures of atmospheric temperatures over a broad altitude range, centered at 0.6 mbar, which corresponds to a height of approximately 26 km [*Kieffer et al.*, 1976b]. Examination of the south polar T_{15} observations obtained during the mapping period showed that they were highest near 17 hours Mars local time, and lowest near 5 hours Mars local time. This is consistent with T_{15} variations observed at most latitudes during nondust storm periods [*Martin and Kieffer*, 1979], and the predictions of the one-dimensional model used in this study. Figure 12 shows latitudinally averaged T_{15} observations obtained midway through the mapping period for emission angles of less than 60° between 4 to 6 hours, and 16 to 18 hours. As in Paper 1, the one-dimensional model-calculated T_{15} values are extremely sensitive to total dust optical depths, to the ratio of visible to infrared dust opacity, and to the dust vertical distribution (see Figure 10h). Of the eight cases investigated, model atmosphere 5 appears to provide the best fit to the T_{15} measurements. As in Paper 1, the one-dimensional model tended to underestimate the amplitudes of diurnal T_{15} variations. The exact cause(s) of this disagreement have not been identified (see Paper 1).

Discussion

The one-dimensional model calculations presented in this section appear to provide reasonable, first-order explanations for

Table 2. One-Dimensional Model-Calculated Quantities for Eight Model Atmospheres at 60°S and 80°S for I=83.72 and A_s=0.25 at L_s=295 From Figure 9

	Latitude 60°S									Latitude 80°S								
	0	1	2	3	4	5	6	7	8	0	1	2	3	4	5	6	7	8
T_{20} min	151.8	174.3	183.0	196.5	180.4	179.0	188.1	190.9	197.7	215.8	226.8	223.2	223.2	219.3	222.1	219.2	221.2	220.1
T_{20} avg	222.9	233.7	232.9	233.5	230.4	232.6	232.3	234.1	232.9	239.3	247.2	243.1	239.3	239.6	243.5	238.9	240.2	235.7
T_{20} max	284.6	286.3	280.8	271.9	278.9	283.9	278.8	279.6	272.1	260.5	265.3	261.1	254.7	258.0	262.8	257.7	258.6	251.6
I^*	84.6	165.4	233.7	397.5	217.1	197.7	272.1	300.7	420.9	88.0	203.7	197.1	297.2	165.4	155.4	172.0	203.7	285.5
A^*	0.25	0.15	0.19	0.22	0.22	0.18	0.21	0.19	0.23	0.24	0.13	0.19	0.23	0.23	0.19	0.25	0.23	0.28
T_s min	151.8	174.3	179.7	189.1	177.5	177.5	183.5	185.3	189.9	215.8	226.8	223.5	221.4	220.0	221.9	216.9	217.8	214.5
T_s avg	222.9	233.7	234.1	235.7	231.9	232.7	231.6	232.5	230.5	239.3	247.2	245.1	242.1	242.0	243.9	238.4	238.8	233.0
T_s max	284.6	286.3	286.0	284.3	284.4	285.4	282.0	282.4	276.3	260.5	265.3	264.5	261.7	261.8	263.7	258.8	259.0	251.7
I_s^*	84.6	165.4	198.7	268.8	183.7	183.7	230.4	248.8	300.7	88.0	203.7	158.7	165.4	141.6	144.9	135.6	148.2	172.0
A_s^*	0.25	0.15	0.16	0.16	0.19	0.17	0.21	0.20	0.25	0.24	0.13	0.17	0.20	0.21	0.18	0.25	0.25	0.32
A_p	0.25	0.25	0.24	0.22	0.26	0.24	0.22	0.21	0.19	0.25	0.25	0.24	0.24	0.28	0.24	0.24	0.24	0.23
T_{15} min	-	177.8	198.0	208.3	191.4	199.5	214.7	197.6	221.9	-	179.5	206.1	220.9	197.3	207.7	228.0	204.3	239.5
T_{15} max	-	179.6	204.5	222.8	196.9	204.9	226.7	200.7	242.4	-	180.1	208.0	224.9	199.0	209.2	230.9	205.3	244.6

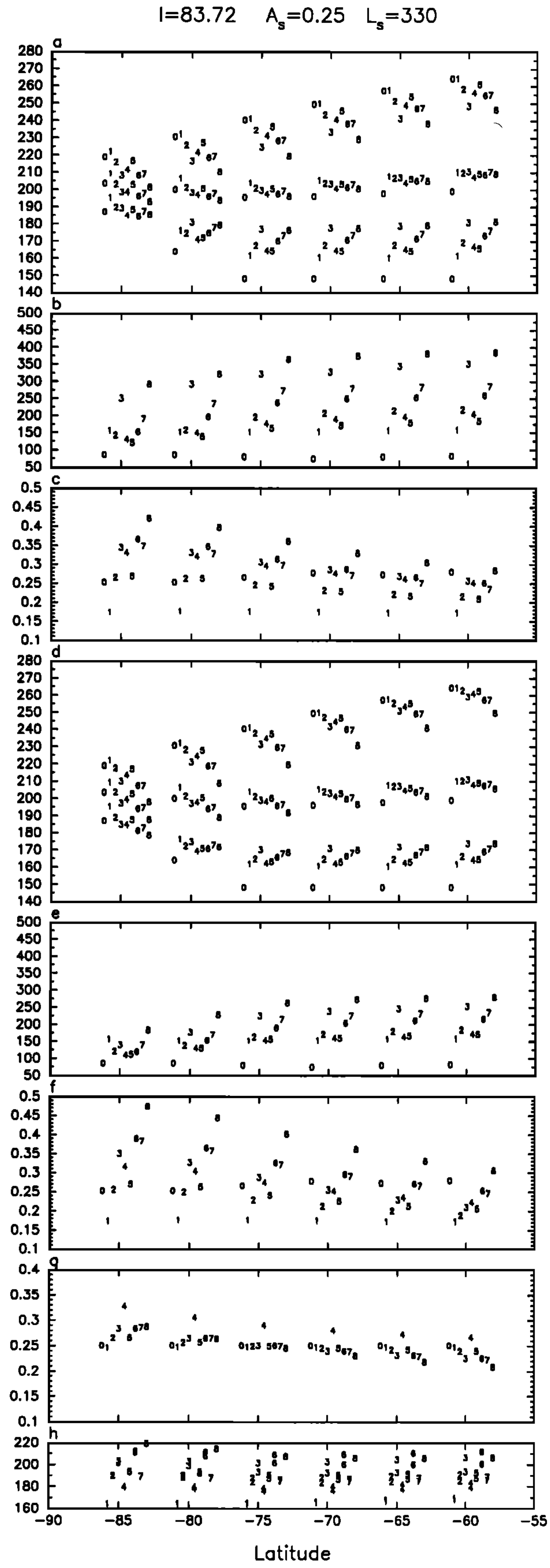

Figure 10. Same as Figure 9 midway through the mapping period at L_S 330. Note different scales on some of the plots.

Table 3. One-Dimensional Model-Calculated Quantities for Eight Model Atmospheres at 60°S and 80°S for I=83.72 and A_s=0.25 at L_s=330 From Figure 10

Latitude 60°S

	0	1	2	3	4	5	6	7	8
T_{20}min	148.0	161.4	169.3	180.7	166.7	165.6	173.2	175.9	181.2
T_{20}avg	198.8	210.0	209.5	210.4	206.9	208.9	208.5	210.2	208.9
T_{20}max	264.1	264.2	258.1	248.1	255.9	260.9	254.4	254.7	246.2
I*	81.3	157.0	217.1	350.8	202.7	183.7	258.8	285.5	384.2
A*	0.28	0.17	0.22	0.26	0.25	0.21	0.25	0.23	0.28
$T_s$min	148.0	161.4	166.1	173.5	163.9	164.2	168.7	170.4	173.5
$T_s$avg	198.8	210.0	210.0	210.8	207.7	208.8	207.2	208.1	205.6
$T_s$max	264.1	264.2	262.7	258.9	260.7	262.2	257.1	257.1	249.5
I_s*	81.3	157.0	183.7	252.1	170.4	170.4	215.4	233.7	278.8
A_s*	0.28	0.17	0.19	0.21	0.22	0.20	0.25	0.25	0.31
A_p	0.25	0.25	0.24	0.22	0.27	0.24	0.22	0.22	0.21
T_{15}min	-	167.8	184.9	193.2	178.6	187.1	200.2	185.7	206.1
T_{15}max	-	169.3	190.6	206.1	183.1	192.0	211.5	188.4	225.5

Latitude 80°S

	0	1	2	3	4	5	6	7	8
T_{20}min	163.8	176.0	174.5	180.8	170.8	171.8	174.6	177.9	179.2
T_{20}avg	199.7	206.2	200.9	198.0	196.8	200.4	195.7	197.5	193.5
T_{20}max	230.4	232.0	225.6	216.4	221.5	227.0	218.3	219.0	210.1
I*	84.6	150.9	157.0	290.6	148.2	137.0	195.4	233.7	320.7
A*	0.25	0.17	0.26	0.33	0.32	0.26	0.35	0.33	0.40
$T_s$min	163.8	176.0	172.1	174.4	169.1	170.6	170.4	172.6	171.5
$T_s$avg	199.7	206.2	201.2	196.9	197.6	200.2	193.8	194.6	188.7
$T_s$max	230.4	232.0	228.1	220.8	224.3	227.6	218.6	218.6	208.7
I_s*	84.6	150.9	137.0	175.4	128.9	128.9	152.0	168.7	227.1
A_s*	0.25	0.17	0.25	0.33	0.30	0.26	0.36	0.36	0.44
A_p	0.25	0.25	0.26	0.26	0.31	0.26	0.26	0.26	0.26
T_{15}min	-	163.8	188.0	198.4	177.9	191.5	207.4	187.1	214.1
T_{15}max	-	164.3	189.8	202.7	179.4	192.9	211.1	187.9	221.7

three major aspects of the south polar thermal and albedo mapping results presented earlier. First, the model results show that the presence of dust in the south polar atmosphere cools the surface, especially near the south pole where solar zenith angles are highest. This can explain the anomalously cold bare-ground surface temperatures observed at the highest latitudes during this season, which are responsible for the anomalously high best fit apparent albedos. Second, atmospheric dust increases apparent thermal inertias, but its effects are likely to be smaller near the south pole than they are at lower latitudes during this season. This can help explain the poleward decrease in observed best fit apparent thermal inertias at all longitudes. Third, the presence of dust gives rise to systematic patterns of residual diurnal variations in measured brightness temperatures at the top of the atmosphere. These calculated patterns of residual diurnal variability agree with those that are observed.

Despite the good agreement between the predictions of the one-dimensional model calculations and the IRTM observations, there are many surface and atmospheric properties that cannot be well constrained. Chief among these are the temperature structure of the atmosphere, the optical depths and the optical properties of the dust at solar and infrared wavelengths, and the vertical distribution of the dust. In the future, more complete and more direct measurements of these quantities should make it possible to refine our understanding of the effects of the Martian atmosphere on the surface heat balance. Because of the apparent sensitivity of south polar surface temperatures to atmospheric effects, the Martian south polar region may serve as a useful laboratory for testing models for similar phenomena, such as the effects of volcanic and man-made aerosols on the surface temperature of the Earth.

4. Interpretation

The maps of apparent thermal inertia and albedo presented in this study provide new information concerning the properties of the surface materials in the south polar region. In this section, we interpret these maps, emphasizing the south residual cap area, the south polar layered deposits, and the stability of water ice. We also consider and reject three alternative explanations for the anomalously cold surface temperatures observed in the dark region surrounding the south residual cap.

South Residual Cap and Vicinity

Previous analyses of Viking observations obtained during the mapping period have made a strong case for the presence of CO_2 frost at the south residual cap [*Kieffer*, 1979; *James et al.*, 1979; *Paige and Ingersoll*, 1985]. The results of this study are completely consistent with this conclusion. The most relevant piece of new information is the near absence of observable diurnal brightness temperature variations in the bright core region of the residual cap (see Figure 7 top).

For the mapping regions that border the south residual cap, the best fit apparent thermal inertias and albedos presented in Plates 1 and 2 are very uncertain (see Figure 2) due to spatially unresolved thermal structure and the possibility of small pointing errors. However, in the disappearing, elongated, bright frost outlier centered at 84°S, 15°W, the maps give evidence for anomalous thermal behavior. This feature is clearly visible in the best fit apparent albedo map in Plate 2, but is not discernible in the Lambert albedo map in Plate 3. Examination of the calculated daily minimum and maximum temperature maps in

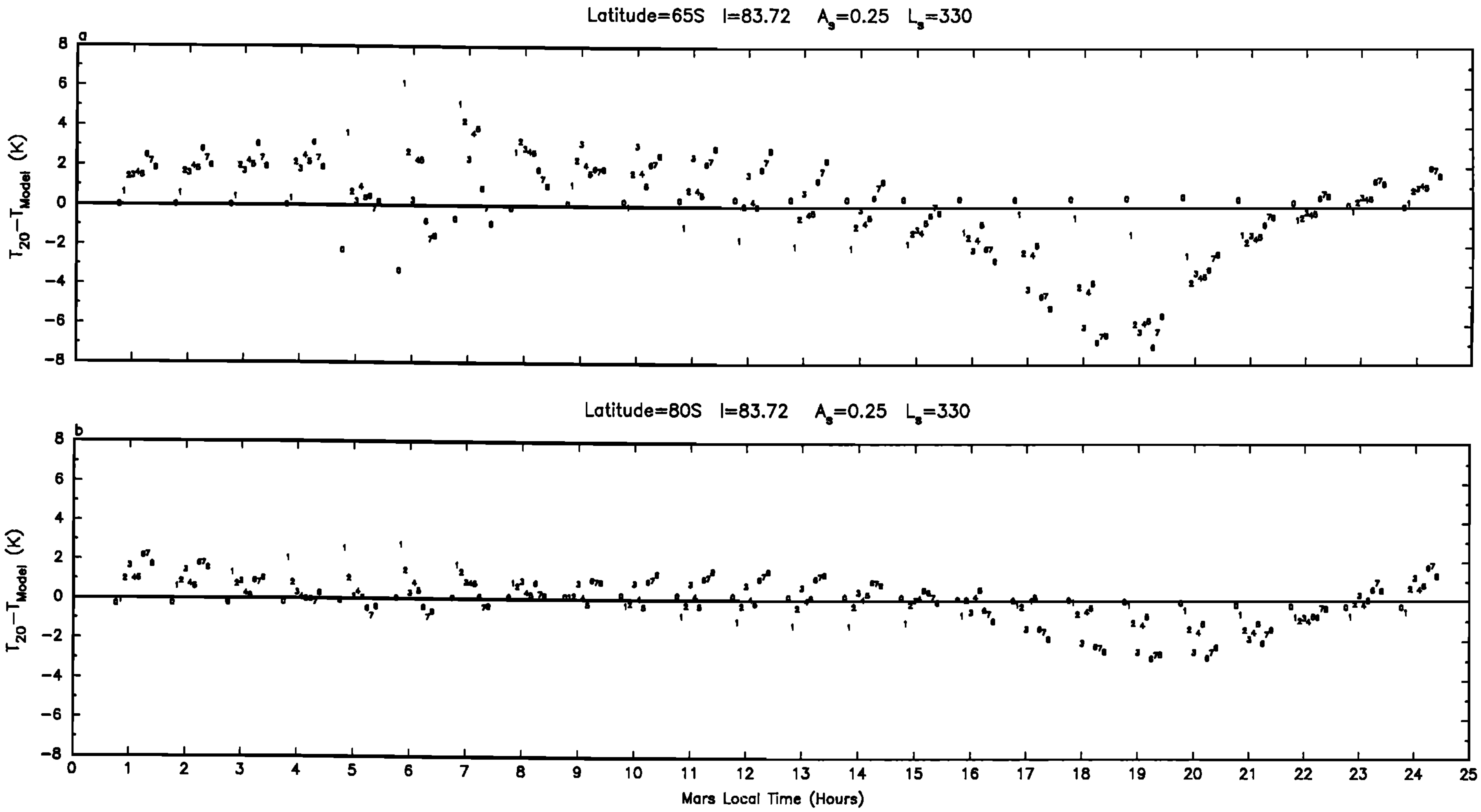

Figure 11. Computed residual diurnal variability due to the effects of the atmosphere midway through the mapping period. Differences between one-dimensional model-calculated IRTM 20-μm channel brightness temperatures at the top of the atmosphere T_{20} and best fit basic thermal model temperatures T_{Model} as a function of Mars local time at (top) 65°S and (bottom) 80°S. Numeric symbols represent the results for the corresponding model atmospheres in Table 1. The symbols are offset horizontally from their true Mars local times, which assume integer values.

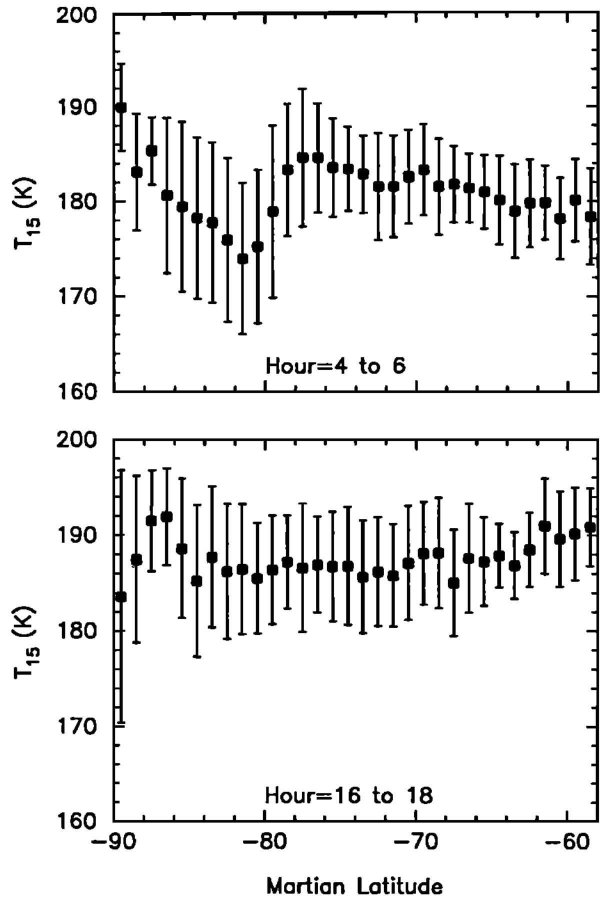

Figure 12. Latitudinally averaged IRTM 15-μm channel brightness temperatures with standard deviations. Plotted are all observations obtained for emission angles of less than 60° between 4 and 6 hours, and 16 and 18 hours.

Plates 5 and 6 show that daily minimum temperatures in the outlier are similar to those in adjacent dark regions, whereas daily maximum temperatures are distinctly lower. The reduced range of diurnal temperature variation observed in the outlier is responsible for its high apparent thermal inertia. The anomalously cold temperatures observed in the outlier region can be easily explained by the presence of patchy, sublimating CO_2 frost in the outlier region. This conclusion is consistent with the results of two previous studies. *Herkenhoff* and *Murray* [1990] have analyzed Viking Orbiter multispectral images obtained just after the end of the mapping period at L_s 341, and found evidence for frost and bare ground mixed well below the resolution of the images in many dark areas adjacent to the cap. Also, a combined analysis of Mariner 9 IRIS spectra and Mariner 9 television camera images provides evidence for the presence of anomalously cold material in dark areas adjacent to the south residual cap [*Paige et al.*, 1990].

In the bare-ground regions extending away from the residual cap to 70°S, measured brightness temperatures continue to be distinctly colder than simple thermal model calculations predict (see Figure 7). In the last section, one-dimensional model calculations showed that this region of anomalously low surface temperatures could be explained in large part by the net cooling effects of dust in the south polar atmosphere. The possible presence of sublimating, patchy CO_2 frost in the area surrounding the south residual cap is an alternate explanation for these anomalously cold surface temperatures. However, this is unlikely for a number of reasons. First, unlike the sublimating frost outlier region described earlier, these darker areas have low apparent thermal inertias, which would not be expected if sublimating CO_2 frost were present. Second, the Viking observations show that the regions along the 225°W meridian became visibly frost free as early as L_s 250, which was more than 100 days before the start of the mapping period. Since these regions were continuously illuminated over a complete range of solar azimuth angles during this period, it is doubtful that any patches of frost could remain. Finally, Viking multispectral images obtained shortly after the mapping period provide no evidence for the presence of surface frost in these areas [*Herkenhoff and Murray*, 1990]. For the sake of completeness, it should also be mentioned that subsurface CO_2 deposits are not likely to be thermally stable beneath unfrosted surface soil layers, because annual average surface and subsurface temperatures in areas that lose their CO_2 cover will be higher than the CO_2 frost point [*Ingersoll*, 1974]. Therefore, for all these reasons, we reject patchy CO_2 frost as an explanation for the anomalously cold surface temperatures.

The Cooling Effects of Sublimation Winds

A second possible explanation for the anomalously cold temperatures observed in the dark region surrounding the south residual cap is that they are due to near-surface sublimation winds. During the mapping period, the south residual cap was still undergoing net CO_2 frost sublimation, which should have been accompanied by a net equatorward flow of cold CO_2 gas away from the cap. Due to the stable stratification of the south polar atmosphere and the high mean molecular weight of the cold CO_2 gas evolved from the cap, the outward flowing condensation wind should, at least initially, be confined close to the surface. The existence of strong, outward flowing surface winds during this season is indicated by observations of dark wind streaks [*Thomas et al.*, 1979] and by dynamical models for the Martian polar vortex [*French and Gierasch*, 1979]. In the analysis presented below, we show that no matter how closely they are confined to the surface, the potential cooling effects of these sublimation winds cannot account for the lower than expected surface temperatures observed in the entire bare-ground region surrounding the south residual cap.

Midway through the mapping period, IRTM radiative balance measurements at the top of the atmosphere indicate that CO_2 frost sublimation at the core region of the south residual polar cap resulted in latent heat storage rates on the order of 20 W m^{-2} [*Paige and Ingersoll*, 1985]. If the south residual polar cap is approximated as a circular region with a radius of 3° of latitude, this would correspond to a whole cap CO_2 gas production rate of 2.9 x 10^6 kg s^{-1} assuming a latent heat of 590,000 J kg^{-1}. The maximum potential surface cooling effect of the resulting condensation wind can be estimated by assuming that the CO_2 gas flows radially into the anomalously cold region surrounding the polar cap at the CO_2 solid-vapor equilibrium temperature of 148 K, exchanges heat with the surface, and then flows radially outward from the region at the radiative equilibrium temperature of 200 K. If the anomalously cold region surrounding the polar cap is approximated as an annulus with a inner diameter of 3° of latitude and an outer diameter of 6° of latitude, the whole cap gas production rate would result in an average surface cooling rate of 0.4 W m^{-2} if the specific heat of the gas is 736 J kg^{-1} K^{-1}. For a surface at 200 K, this cooling rate would result in a decrease in its equilibrium surface temperature by only a few tenths of a Kelvin, which is much smaller than the observed cooling effect in this region, which is approximately 10 K. Therefore, we reject sublimation winds as an explanation for the anomalously cold surface temperatures.

South Polar Layered Deposits

Determining the thermal inertia of the south polar layered deposits is a key objective of this study. In Paper 1, the north polar layered deposits were shown to have very high thermal inertias, which was interpreted as strong evidence of the presence of near-surface water ice. In the south, polar layered deposits are exposed over a broad region. Figure 13 shows an adaptation of the *Tanaka and Scott* [1987] geologic map of the south polar region of Mars from *Thomas et al.* [1992]. In some areas, the boundaries of the south polar layered deposits are not defined by sharp contacts with adjacent units [e.g., *Murray et al.*, 1972; *Thomas and Weitz*, 1989], but in the vicinity of Chasma Australe near 80°S, 270°W, the boundary is unmistakable. Comparing the *Tanaka and Scott* [1987] map with the south polar apparent thermal inertia map Plate 1 shows little correlation between the locations of south polar thermal inertia features and the locations of south polar deposits, layered or otherwise. The most significant trend that is displayed in the best fit apparent thermal inertia map is a general decrease in apparent thermal inertia from 60°S to the south pole. As discussed in the last section, this could be due largely to the effects of the atmosphere. For a constant dust optical depth, the model results predict that apparent thermal inertias close to the south pole can be significantly lower than apparent thermal inertias at lower latitudes (see Figure 10b). Unfortunately, without more detailed information concerning the structure and dust loading of the south polar atmosphere, it is difficult to determine the extent to which the observed poleward decrease in apparent thermal inertia is due to surface effects,

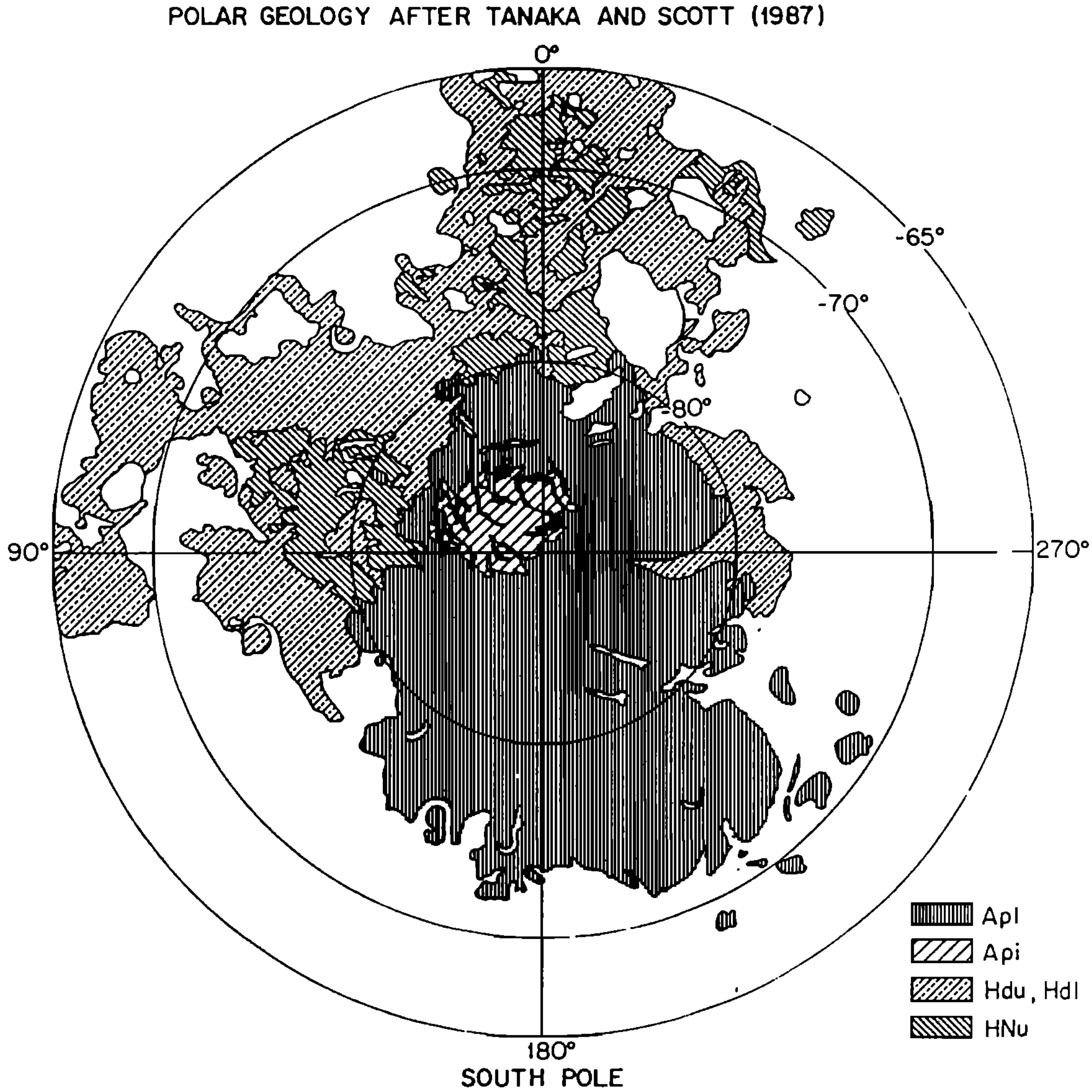

Figure 13. An adaptation of the *Tanaka and Scott* [1987] geologic map of the south polar region of Mars from *Thomas et al.* [1992]. The units are as follows: Apl is polar layered deposits; Api is residual ice; Hdu and Hdl are upper and lower members of the Dorsa Argentea Formation, which are interpreted as aeolian mantle or volcanic deposits; HNu is nonlayered pitted and degraded material mostly underlying the Dorsa Argentea Formation. Blank areas are plains units that have no specific polar associations.

atmospheric effects, or both. However, since the atmosphere will always tend to increase apparent thermal inertias, the inertias derived from the IRTM observations in Plate 1 can be considered upper limits for true surface thermal inertias.

The apparent thermal inertias of the south polar layered terrains place new constraints on the physical properties of the materials that comprise their uppermost surfaces. In Plate 1, the 305 mapping regions that are completely within the area mapped by *Tanaka and Scott* [1987] as south polar layered deposits have an average apparent thermal inertia of approximately 168 J m^{-2} $s^{-1/2}$ K^{-1}. This is considerably lower than the average apparent thermal inertia of the exposed layered deposits in the north (see Paper 1), and compares favorably with the average apparent thermal inertias of the northern midlatitude low thermal inertia regions [*Palluconi and Kieffer*, 1981]. Near the south pole, the apparent thermal inertias are among the lowest mapped anywhere on the planet. Based on the two-layer thermal model calculations presented in Paper 1, these low apparent thermal inertias require the presence of low thermal inertia material that extends from the surface, to depths of at least one half a diurnal skin depth below the surface. For a surface layer thermal inertia of 100 J m^{-2} $s^{-1/2}$ K^{-1}, this would correspond to a minimum thickness of approximately 1 cm.

The most straightforward explanation for the low apparent thermal inertias of the south polar layered deposits is that they are mantled by a layer of aeolian material. Unfortunately, because of uncertainties introduced by the effects of the atmosphere, and uncertainties in the mapping between thermal inertia and particle size (see Paper 1), the exact nature of this mantling material is difficult to determine. Based on the apparent thermal inertia measurements themselves, the region near the south pole of Mars appears to have much in common with the low thermal inertia regions in Tharsis, Arabia, and Elysium, which have been widely interpreted to be uniformly mantled by dust [*Christensen*, 1982]. The existence of a dust mantle on the south polar layered deposits is strongly supported by the results of an analysis of multispectral Viking Orbiter images of regions adjacent to the south residual cap by *Herkenhoff and Murray* [1990], which show that many areas of the south polar layered terrains have very high red to violet reflectance ratios, which are characteristic of dust-covered areas elsewhere on the planet [*Thomas and Veverka*, 1986].

The origin and evolution of the south polar dust mantle are difficult to constrain. The absence of observable outcrops of high thermal inertia material in this region implies that the dust mantle is more than a few millimeters thick. This also suggests that the dust mantle formed, and has existed, over multiyear timescales or longer. Due to the potentially large effects of the atmosphere during the mapping period, the exact boundaries of the dust mantle are difficult to determine. Nonetheless, the fact that there are no distinct thermal inertia boundaries associated with the boundaries of the south polar layered deposits is important. One possibility is that, like the Tharsis, Arabia, and Elysium regions, the south polar region is a favorable location for the deposition and retention of atmospheric dust under present climatic conditions. Atmospheric circulation patterns, the region's high surface elevation, the presence of seasonal CO_2 frost during much of the year, or particle cementing due to the presence of near-surface ground ice could all contribute to the stability of dust deposits at the south pole. If this were true, then the deposition of polar dust layers that are thick enough to be visible in orbital images may not necessarily require climatic conditions that are thought to occur during periods of high obliquity [*Toon et al.*, 1980]. Another possibility is that portions of the south polar layered deposits are not actively forming, but contain "fossil" remnants that were deposited millions or billions of years ago, a notion that is supported by the identification of impact craters [*Plaut et al.*, 1988] and areas of pitted and stripped terrain [*Sharp*, 1973; *Howard et al.*, 1982].

The existence of a low thermal inertia region at the south pole is an intriguing new piece of information. At the present time, the processes responsible for the creation of this deposit are at least as mysterious as those responsible for the creation of low thermal inertia deposits elsewhere on Mars. The location of this deposit close to the south pole lends credence to suggestions that "polar-like" processes such as dust scavenging by precipitating water ice and CO_2 particles [*Palluconi and Kieffer*, 1981] or near-surface ground ice formation [*Paige*, 1992] may play an important role in the origin and evolution of surficial dust deposits planetwide.

The Stability of Water Ice

One of the primary differences between the Martian north and south polar regions is the abundance of surface water ice. In the north polar region, bright water ice is exposed on the surface of the north residual polar cap, and in detached bright outliers [*Kieffer et al.*, 1976a; *Farmer et al*, 1976]. The results of Paper 1 showed that these deposits have very high thermal inertias, which are consistent with the presence of dense, compacted snow or solid ice. The results of Paper 1 also showed that the dark polar layered deposits surrounding the north residual cap also have very high thermal inertias, and were also interpreted to contain near-surface water ice. This conclusion was supported by comparisons between estimates of the water vapor holding capacity of the polar atmosphere based on IRTM surface and atmospheric temperature measurements, and simultaneously acquired Viking Mars atmospheric water detector (MAWD) measurements of the atmospheric column water vapor content. In the south polar region, the Viking observations give little direct evidence for the presence of water ice. At the south residual cap, measured brightness temperatures remained close to the CO_2 frost point throughout the summer season [*Kieffer*, 1979]. In the south polar atmosphere, measured column water vapor abundances never exceeded 15 precipitable microns (pr.-μm) [*Davies and Wainio*, 1981], which is much less than the atmosphere's potential water vapor holding capacity [*Davies et al.*, 1977]. These small water vapor abundances are not consistent with the presence of a water ice reservoir in radiative equilibrium and in good contact with the south polar atmosphere [*Davies and Wainio*, 1981].

The absence of observable surface water ice deposits, or large atmospheric water vapor abundances does not necessarily imply that the region surrounding the south residual cap is completely devoid of water. Mars thermal model calculations dating back more than 25 years show that subsurface soil layers in the south polar region are among the coldest on the planet, and therefore, are likely locations for ground ice deposits [*Leighton and Murray*, 1966; *Farmer and Doms*, 1979; *Zent et al*, 1986; *Paige*, 1992]. Figure 14 shows basic thermal model calculated annual minimum and annual maximum temperatures as a function of latitude and depth in the south polar region. The calculations assume a depth-independent thermal inertia of 100 J m^{-2} $s^{-1/2}$ K^{-1}, a volume heat capacity of 10^6 J m^{-3}, a surface albedo of 0.25, a CO_2 frost albedo of 0.55, and a heat flow rate from the Martian interior of 0.030 W m^{-2}. These parameters provide a reasonably good match to observed surface temperature variations at 80°S

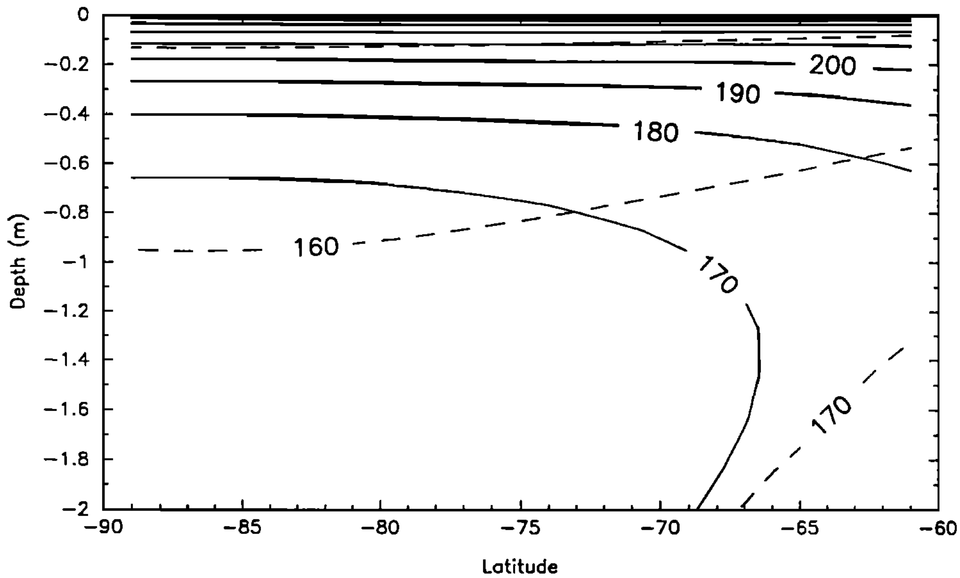

Figure 14. Basic thermal model calculated annual maximum (solid lines) and annual minimum (dashed lines) temperatures assuming a surface albedo of 0.25, a CO_2 frost albedo of 0.55, and a depth-independent thermal inertia of 100 J m^{-2} $s^{-1/2}$ K^{-1}. Water ice should be stable to evaporation in regions with maximum annual temperatures below 198 K.

during the mapping period. The calculated subsurface temperatures can be used to estimate the expected depths of ground ice deposits because near-surface ground ice will not be stable to evaporation if its temperature exceeds the local frost point temperature for an extended period [*Leighton and Murray*, 1966; *Farmer and Doms*, 1979; *Paige*, 1992]. During southern summer, the maximum observed column water vapor abundance in the south polar region was approximately 15 pr.-μm [*Davies and Wainio*, 1989]. If this water vapor were distributed uniformly with pressure, the surface frost point temperature would be approximately 198 K. Since equilibrium vapor pressure is an exponential function of temperature, this assumed maximum surface frost point temperature is relatively insensitive to assumptions concerning vertical water vapor profiles or the effects of atmospheric dust on the MAWD column abundances. This same frost point temperature has been assumed in previous studies to be characteristic of the planet as a whole [*Farmer and Doms*, 1979; *Paige*, 1992]. The thermal model calculations in Figure 14 show that soil temperatures in the south polar region are only expected to exceed 198 K close to the surface. At depths of greater than 20 cm, subsurface temperatures remain below the frost point temperature throughout the year. While there can be little doubt that temperature plays a crucial role in determining the present distribution of ground ice on Mars, other factors, such as regolith adsorption [*Zent et al.*., 1986], soil diffusivity, and history may also be important [*Toon et al.*, 1980; *Hofstadter and Murray*, 1990; *Mellon and Jakosky*, 1993]. Nonetheless, the results of this simple model suggest that near-surface water ice in excellent diffusive contact with the atmosphere could be stable in this region and not be inconsistent with the MAWD observations.

Depending on their depths, the presence of near-surface, high thermal inertia ice deposits might be expected to have measurable effects on surface temperatures. In Paper 1, a series of two-layer thermal model calculations showed that a thin surface layer of low thermal inertia material can "mask" the diurnal thermal inertia signature of high thermal inertia material at depth as long as the thickness of the surface layer is greater than half the diurnal skin depth. While the IRTM observations of large diurnal temperature variations in the region surrounding the residual cap can effectively preclude the presence of high thermal inertia surface ice, they cannot exclude the possibility that high inertia ice lies close to the surface. *Paige* [1992] has shown that ground ice deposits can be stable much closer to the surface than is suggested by the results of simple models that assume vertically homogeneous bulk thermal properties. Once formed at depth, the high thermal inertia ground ice reduces the amplitudes of temperature variations in overlying soil layers, which can promote the formation of more high inertia ground ice closer to the surface [*Paige*, 1992]. Figure 15 shows calculated daily minimum, maximum, and average temperatures during the southern summer season at 80°S. The solid lines show calculated surface temperatures using the basic thermal model assuming a surface albedo of 0.25, a CO_2 frost albedo of 0.55, and a low, depth-independent thermal inertia of 100 J m^{-2} $s^{-1/2}$ K^{-1}. These are the same parameters used in Figure 14. Figure 15 also shows the results of a more elaborate calculation which also assumed these same parameters initially, but as the calculations progressed, subsurface layers with daily maximum temperatures below the assumed frost point temperature of 198 K were gradually increased to simulate the formation of ground ice. The maximum ice-saturated thermal inertia was 1130 J m^{-2} $s^{-1/2}$ K^{-1} and the timescale for complete ice saturation was 20 years [*Paige*, 1992]. After 60 years, the upper surface of the high thermal inertia ice-saturated soil stabilized at 4.1 cm below the surface, which is approximately 2.5 times the diurnal skin depth in the low thermal inertia surface layer. For this set of input parameters, this is the closest to the surface that thermally stable ground ice could exist at this latitude. The dot-dashed lines show calculated surface temperatures, the dashed lines show calculated subsurface temperatures at the top of the high thermal inertia

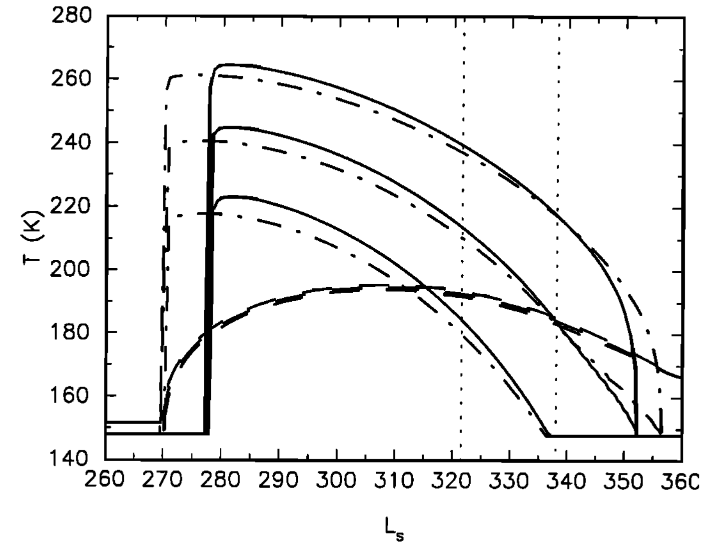

Figure 15. Calculated daily minimum, maximum, and average temperatures at 80°S as a function of L_s during the southern summer season. The solid lines are basic thermal model calculated surface temperatures assuming a surface albedo of 0.25, a CO_2 frost albedo of 0.55, and a depth-independent thermal inertia of 100 J m^{-2} s$^{-1/2}$ K^{-1}. The dot-dashed lines show calculated surface temperatures for a model that used the same surface soil properties, but used time and depth dependent subsurface thermal inertias to simulate the formation of high thermal inertia ground ice as described in the text. The dashed lines show calculated temperatures at the top of the high thermal inertia subsurface ice deposit at a depth of 4.1 cm below the surface. The mapping period is indicated by the vertical dashed lines.

ground ice layer 4.1 cm below the surface. For this case, the complete disappearance of 148 K seasonal CO_2 frost occurs earlier in the season than in the homogeneous case because higher subsurface thermal inertias increase seasonal subsurface heat storage, which decreases the net rate of seasonal CO_2 frost accumulation during the fall and winter seasons [*Paige and Ingersoll*, 1985; *Jakosky and Haberle*, 1990; *Wood and Paige*, 1992]. Figure 15 shows that the potential presence of high thermal inertia ground ice in close proximity to the surface has little effect on the amplitudes of diurnal temperature variations. Its major effect is to decrease average surface temperatures during the early summer, and to increase daily average temperatures during late summer. The presence of near-surface ground ice could potentially be considered as a third explanation of the anomalously cold bare-ground surface temperatures in the vicinity of the south residual cap. However, by the time of the mapping period, which occurred late in the summer season, the apparent ice cooling effect was less than 3 K, which is much less than observed. Given the demonstrably large effects of the atmosphere on the net surface heat balance throughout the summer at these latitudes, it seems doubtful that surface temperature data alone could be used to unambiguously detect the presence of ground ice. Figure 15 shows that at a depth of 4.1 cm below the surface, temperatures remained lower than 198 K throughout the year. This means that if ground ice deposits were present at these depths, and in good contact with the atmosphere, their vapor pressures would be consistent with the MAWD water vapor observations during this season.

In summary, the MAWD and IRTM observations of the Martian north and south polar regions during their respective summer seasons appear to paint a consistent picture. In the north, regions with high atmospheric water vapor abundances are associated with regions of high thermal inertia, which is consistent with the presence of surface water ice. In the south, there are no regions of high atmospheric water abundances, and no regions with high thermal inertia, which is consistent with an absence of surface water ice. The low atmospheric water vapor abundances observed in the south do not necessarily imply a complete absence of water ice because subsurface temperatures and observed atmospheric water abundances permit the thermal stability of ground ice deposits, even if they are excellent diffusive contact with the atmosphere.

5. Conclusions

The principal conclusions of this study are as follows.

1. The apparent thermal inertias of bare-ground regions systematically decrease from 60°S to the south pole. Close to the south pole, apparent thermal inertias are among the lowest observed anywhere on the planet. The region of low apparent thermal inertia includes the south polar layered deposits.

2. The apparent thermal inertia of the south residual polar cap is extremely high due to the presence of CO_2 frost.

3. During the late summer season, best fit apparent albedos are systematically higher than measured Lambert albedos poleward of 75°S, implying that measured brightness temperatures in this region are up to 15 K colder than would be expected for surfaces with the same measured albedos. These anomalously cold brightness temperatures cannot be satisfactorily explained by the presence of patchy CO_2 frost, subsurface CO_2 frost, polar cap sublimation winds, or the thermal effects of high inertia ground ice.

4. The anomalously cold brightness temperatures can be satisfactorily explained by the radiative effects of dust in the south polar atmosphere during the late summer season. One-dimensional atmospheric radiative-convective model calculations show that the tendency for dust to cool the surface is enhanced for high dust opacities, high solar zenith angles, and low visible-to-infrared dust opacity ratios. For a constant dust optical depth, these same atmospheric model calculations also predict a systematic decrease in apparent thermal inertia from 60°S to the south pole.

5. The low apparent thermal inertias that are mapped close to the south pole imply that the region is mantled by a continuous layer of aeolian material that is at least a few millimeters thick. This conclusion is supported by the results of an analysis of multispectral Viking Orbiter images of regions adjacent to the south residual cap [*Herkenhoff and Murray*, 1990]. The south polar low thermal inertia region may be analogous to the north temperate low thermal inertia regions in Tharsis, Arabia, and Elysium.

6. The low thermal inertias that are mapped in the south polar region imply an absence of surface water ice, which is consistent with the Viking MAWD observations of low atmospheric water vapor abundances throughout the summer season.

7. The absence of surface ice and low water vapor abundances does not necessarily imply that the south polar region is devoid of water. Thermal model calculations show that annual maximum subsurface temperatures at depths ranging from 4 to 20 cm below the surface never exceed 198 K at any time during the summer season. This implies that the presence of stable ground ice

deposits at these depths in good diffusive contact with the atmosphere would not result in water vapor abundances higher than those observed by MAWD.

Acknowledgments. We thank the Viking IRTM team for a acquiring and archiving a superb data set. We thank Bruce Jakosky, Hugh Kieffer, Frank Palluconi, and Richard Zurek for many helpful discussions and suggestions, and Robert Haberle and Ken Herkenhoff for thorough and constructive reviews of this manuscript. We also thank Carol Chang for programming assistance, and the JPL Multiple Mission Image Processing Lab for hard copy of the color figures, and Karen McBride-Bei for typesetting this manuscript. This research was supported by the NASA Planetary Geology and Geophysics Program.

References

Cess, R. D., G. L. Potter, S. J. Ghan, and W. L. Gates, The climatic effects of large injections of atmospheric smoke and dust: A study of climate feedback mechanisms with one- and three-dimensional models, *J. Geophys. Res, 90*, 12,937-12,950, 1985.

Chase, S. C., J. L. Engle, H. W. Eyerly, H. H. Kieffer, F. D. Palluconi , and D. Schofield, Viking infrared thermal mapper, *Appl. Opt., 17*, 1243-1251, 1978.

Christensen, E. J., Martian dust mantling and surface composition: Interpretation of thermophysical properties, *J. Geophys. Res. 87*, 9985-9998, 1982.

Clancy, R. T., and S. W. Lee, A new look at dust and clouds in the Mars atmosphere-Analysis of emission-phase-function sequences from global Viking IRTM observations, *Icarus, 93*, 135-158, 1991.

Davies, D. W., Effects of dust on the heating of Mars' surface and atmosphere, *J. Geophys. Res., 84*, 8289-8293, 1979.

Davies, D. W., and L. A. Wainio, Measurements of water vapor in Mars' antarctic, *Icarus, 45*, 216-230, 1981.

Davies, D. W., C. B. Farmer, and D. D. La Porte, Behavior of volatiles in Mars' polar areas: A model incorporating new experimental data, *J. Geophys. Res., 82*, 3815-3822, 1977.

Deirmendjian, D., *Electromagnetic Scattering of Spherical Polydispersions*, Elsevier, New York, 1969.

Ditteon, R., Daily temperature variatins on Mars, *J. Geophys. Res., 87*, 10,197-10,214, 1982.

Farmer, C. B., and P. E. Doms, Global seasonal variation of water vapor on Mars and the implications for permafrost, *J. Geophys. Res., 84*, 2881-2888, 1979.

Farmer, C. B., D. W. Davies and D. D. LaPorte, Mars: Northern summer ice cap-water vapor observations from Viking 2, *Science, 194*, 1339-1341, 1976.

French, R. G., and P. J. Gierasch, The Martian polar vortex: Theory of seasonal variation and observations of eolian features, *J. Geophys. Res., 84*, 4634-4642, 1979.

Haberle, R. M., and B. M. Jakosky, Atmospheric effects on the remote determination of thermal inertia on Mars, *Icarus, 90*, 187-204, 1991.

Hansen, J. E., and L. D. Travis, Light scattering in planetary atmospheres, *Space Sci. Rev., 16*, 527-610, 1974.

Herkenhoff, K. E., and B. C. Murray, Color and albedo of the south polar layered deposits on Mars, *J. Geophys. Res., 95*, 1343-1358, 1990.

Hofstadter, M. D. and B. C. Murray, Ice sublimation and rheology: Implications for the Martian polar layered deposits, *Icarus, 84*, 352-361, 1990.

Hunt, G. E., Thermal infrared properties of the Martian atmosphere, 4, Prediction of the presence of dust and ice clouds from Viking IRTM spectral measurements, *J. Geophys. Res., 84*, 2865-2874, 1979.

Ingersoll, A.P., Mars: The case against permanent CO_2 frost caps, *J. Geophys. Res., 79*, 3403-3410, 1974.

Jakosky, B. M., and E. S. Barker, Comparison of ground-based and Viking Orbiter measurements of martian water vapor: Variability of the seasonal cycle, *Icarus, 57*, 322-332, 1984.

Jakosky, B. M., and R. M., Haberle, Year to year instability of the Mars south polar cap, *J. Geophys. Res., 95*, 1359-1365, 1990.

James, P. B., G. Briggs, J. Barnes, and A. Spruck, Seasonal recession of Mars' south polar cap as seen by Viking, *J. Geophys. Res., 84*, 2889-2922, 1979.

Kieffer, H. H., Mars south polar spring and summer temperatures: A residual CO_2 frost, *J. Geophys. Res., 84*, 8263-8288, 1979.

Kieffer, H. H., S. C. Chase Jr., T. Z. Martin, E. D. Miner, and F. D. Palluconi, Martian north pole summer temperatures: Dirty water ice, *Science, 194*, 1341-1344, 1976a.

Kieffer, H. H., P. R. Christensen, T. Z. Martin, E. D. Miner, and F. D. Palluconi, Temperatures of the Martian surface and atmosphere: Viking observation of diurnal and geometric variations, *Science, 194*, 1346-1351, 1976b.

Kieffer, H. H., T. Z. Martin, A. R. Peterfreund, B. M. Jakosky, E. D. Miner, and F. D. Palluconi, Thermal and albedo mapping of Mars during the Viking primary mission, *J. Geophys. Res,. 82*, 4249-4291, 1977.

Leighton, R. B., and B. C. Murray, Behavior of carbon dioxide and other volatiles on Mars, *Science, 153*, 136-144, 1966.

Martin, T. Z., and H. H. Kieffer, Thermal infrared properties of the Martian atmosphere, 2, The 15 micron band measurements, *J. Geophys. Res., 84*, 2843-2852, 1979.

Martin, T. Z., A. R. Peterfreund, E. D. Miner, H. H. Kieffer, and G. E. Hunt, Infrared properties of the Martian atmosphere 1. Global behavior at 7, 9, 11, and 20 microns, *J. Geophys. Res., 84*, 2830-2842, 1979.

Mellon, M. T., and B. M. Jakosky, Geographic variations in the thermal and diffusive stability of ground ice on Mars, *J. Geophys. Res., 98*, 3345-3364, 1993.

Murray, B. C., L. A. Soderblom, J. A. Cutts, R. P. Sharp, D. J. Milton, and R. B. Leighton, Geological framework of the south polar region of Mars, *Icarus, 17*, 328-345, 1972.

Paige, D. A., The thermal stability of near-surface ground ice on Mars, *Nature, 356*, 43-45, 1992.

Paige, D. A., and A. P. Ingersoll, Annual heat balance of Martian polar caps: Viking observations, *Science, 228*, 1160-1168, 1985.

Paige, D. A., K. E. Herkenhoff, and B. C. Murray, Mariner 9 observations of the south polar cap of Mars: Evidence for residual CO_2 frost, *J. Geophys. Res., 95*, 1319-1335, 1990.

Paige, D. A., J. E. Bachman, and K. D. Keegan, Thermal and albedo mapping of the polar regions of Mars using Viking thermal mapper observations, 1, North polar region, *J. Geophys. Res.*, this issue.

Palluconi, F. D., and H. H. Kieffer, Thermal inertia mapping of Mars from 60°S to 60°N, *Icarus, 45*, 415-426, 1981.

Pleskot, L. K., and E. D. Miner, Time variability of Martian bolometric albedo, *Icarus, 50*, 259-287, 1982.

Pollack, J. B., O. B. Toon, and B. N. Khare, Optical properties of some terrestrial rocks and glasses, *Icarus, 19*, 372-389, 1973.

Pollack, J. B., D. S. Colburn, F. M. Flasar, R. Kahn, C. E. Carlston, and D. Pidek, Properties and effects of dust particles suspended in the Martian atmosphere, *J. Geophys. Res., 84*, 2929-2945, 1979.

Tanaka, K. L., and D. H. Scott, Geologic map of the polar regions of Mars, Atlas of Mars, 1:15,000,000, *Geol. Ser., I-1802-C*, U.S. Geol. Surv., Reston, Va.,1987.

Thomas, P. J. and J. Veverka, Red/Violet contrast reversal on Mars: Significance for eolian sediments, *Icarus, 66*, 39-55, 1986.

Thomas, P. J. and C. Weitz, Sand dune materials and polar layered deposits on Mars, *Icarus, 81*, 185-215, 1989.

Thomas, P., J. Veverka, and R. Campoos-Marquetti, Frost streaks in the south polar cap of Mars, *J. Geophys. Res., 84*, 4621-4632, 1979.

Thomas, P., K. E. Herkenhoff, A. D. Howard, B. C. Murray, and S. L. Squyres, Polar deposits of Mars, in *Mars*, University of Arizona Press, Tucson, 1992.

Toon, O. B., J. B. Pollack, and C. Sagan, Physical properties of the particles composing the Martian dust storm of 1971-2, *Icarus, 30*, 663-696, 1977.

Toon, O. B., J. B. Pollack, W. Ward, J. A. Burns and K. Bilski, The astronomical theory of climatic change on Mars, *Icarus, 44*, 552-607, 1980.

Turco, R. P., O. B. Toon, T. P. Ackerman, J. B. Pollack, and C. Sagan, Nuclear winter: Physics and physical mechanisms, *Annu. Rev. Earth Planet. Sci.*, *19*, 383-422, 1991.

Wood, S. E., and D. A. Paige, Modeling the Martian seasonal CO_2 cycle, 1, Fitting the Viking lander pressure curves, *Icarus*, *99*, 1-14, 1992.

Zent, A. P., F. P. Fanale, J. R. Salvail, and S. E. Postawko, Distribution and state of H_2O in the high-latitude shallow subsurface of Mars, *Icarus*, *67*, 19-36, 1986.

Zurek, R. W., Martian great dust storms: An update, *Icarus*, *50*, 288-310, 1982.

K. D. Keegan and D. A. Paige, Department of Earth and Space Sciences, University of California, Los Angeles, Los Angeles, CA 90024.

(Received August 31, 1992; revised October 15, 1993; accepted December 3, 1993.)